Analytical sensitivity analysis of flexible aircraft with the unsteady vortex-lattice aerodynamic theory

Xiaochen Hang [a,1], Weihua Su [b,2], Qingguo Fei [a,*,3], Dong Jiang [c,4]

[a] *Southeast University, Nanjing, Jiangsu, 210096, China*
[b] *The University of Alabama, Tuscaloosa, AL, 35487-0280, United States*
[c] *Nanjing Forestry University, Nanjing, Jiangsu, 210037, China*

ARTICLE INFO

ABSTRACT

The unsteady vortex-lattice method provides a medium-fidelity tool for calculation of low-speed aerodynamic loads based on the potential-flow theory. It has long been favored in research on the aeroelasticity and flight dynamics for flexible aircraft with high aspect ratios. However, the unsteady vortex-lattice method is established in the discrete time domain which brings difficulties to modeling aeroelastic system for stability analysis. An analytical aerodynamic sensitivity calculation scheme is developed in this paper to formulate the aeroelastic equations of motion with UVLM aerodynamics. A free wake model is used to simulate accurate vortex shedding and subsequent wake propagation. Using a small perturbation method, the aerodynamic governing equations are linearized around the equilibrium condition, where the analytical sensitivities can be derived. The surface spline interpolation algorithm is adopted to implement the structure-aerodynamic coupling. Both aerodynamic sensitivities with respect to structural motions and circulation strengths of vortices are obtained. In numerical studies, a time-marching transient response analysis scheme is used to obtain the distributed aerodynamic loads and structural deformations. Analytical sensitivity results are validated by the finite difference method. The proposed analytical sensitivity calculation framework is demonstrated to be applicable to commonly used beam-based flexible wing models, as well as the shell-based finite element models with higher fidelity. The derived sensitivity formulations and related numerical implementations can build the foundation for further studies on aeroelastic optimization and stability analysis.

1. Introduction

Unsteady aerodynamics has long played a critical role in problems like aircraft design, aeroelastic stability analysis, and multidisciplinary optimization. In low airspeed regime particularly, simple aerodynamic approaches like strip theory are still used commonly at the conceptual design stage of an aircraft [1]. With a relatively higher fidelity, unsteady aerodynamic theories based on potential-flow theories such as the doublet-lattice method [2] (DLM) provide reliable predictions of non-stationary aerodynamics for subsonic aeroelasticity. Computational fluid dynamics (CFD) has furnished the high-fidelity tool for aerodynamic predictions in recent decades [3–8]. CFD-based methods originally focused on static aerodynamics only, with the assumption of rigid structures. Aerodynamic loads were linear with a change of structural displacements and angle of attack. Later on, although elastic structural models were coupled with CFD tools to predict unsteady aerodynamics, linearization hypothesis and Reduced Order Model (ROM) were employed to improve the computational efficiency. However, as the unmanned aerial vehicles (UAV) especially high-altitude long-endurance (HALE) aircraft become more and more popular [9–14], these aerodynamic tools show their disadvantages and may be no longer suitable for modeling accurate unsteady aerodynamics efficiently. HALE aircraft feature wings with high aspect-ratio, which maximizes the lift-over-drag ratio to improve overall efficiency. They usually consist of very light, slender and thus flexible structures, which may cause geometrically nonlinear deformations during normal operation and overlap of the aeroelastic and rigid-body frequencies. Therefore, for HALE vehicles, any successful modeling effort requires the aerodynamic approach to be incorporated with structures that have large nonlinear deformations and multidisciplinary coupling.

* Corresponding author.
E-mail addresses: hangxiaochen@seu.edu.cn (X. Hang), suw@eng.ua.edu (W. Su), qgfei@seu.edu.cn (Q. Fei), jiangdong@njfu.edu.cn (D. Jiang).
[1] Department of Engineering Mechanics.
[2] Department of Aerospace Engineering and Mechanics.
[3] School of Mechanical Engineering.
[4] School of Mechanical and Eletronic Engineering.

Nomenclature

a	distance from the elastic axis to the mid-point of the wing section
$\mathbf{A}_b$, $\mathbf{A}_w$	sparse matrix in wake circulation propagation equation
b_k	spanwise length of aerodynamic panel k
$\mathbf{B}_b$, $\mathbf{B}_w$	sparse matrix in propagation equation for wake grid points
c_k	chordwise length of aerodynamic panel k
$\mathbf{C}$	structural damping matrix
$\mathbf{D}$	aerodynamic drag force
$\mathbf{E}_1$, $\mathbf{E}_2$	sparse matrices in formula of aerodynamic loads
$\mathbf{F}$	aerodynamic loads include lift and drag
$\mathbf{G}_1$, $\mathbf{G}_2$	matrices in formula of aerodynamic loads
$\mathbf{H}$	system matrix in state-space equation
$\mathbf{K}$	structural stiffness matrix
$\mathbf{L}$	aerodynamic lift force
m	number of chordwise panels
$\mathbf{M}$	structural mass matrix
n	number of spanwise panels
$\mathbf{n}$	normal vectors of aerodynamic panels
$\mathbf{p}_a$, $\mathbf{p}_b$, $\mathbf{p}_1$, $\mathbf{p}_2$	coordinate of a single point
$\triangle p_{m,n}$	pressure on each bound panel
$\mathbf{q}$	velocity vector induced by a vortex segment

$\mathbf{r}$	vector in space
$\mathbf{T}$	interpolation matrix between structural nodes and bound vortex panels
$\mathbf{u}^w$	wake induced velocity at collocation points
$\mathbf{U}$	non-circulatory velocity at all collocation points
$\mathbf{U}_1$, $\mathbf{U}_2$, $\mathbf{U}_3$	weighted velocity matrix
$\mathbf{W}_{bb}$	influence matrix of bound vortex rings to all collocation points
$\mathbf{W}_{bw}$	influence matrix of wake vortex rings to all collocation points
$\mathbf{X}_s$, $\dot{\mathbf{X}}_s$	structural displacement and velocity matrix
α	angle of attack
$\boldsymbol{\tau}^c$	chordwise tangential vector of an aerodynamic panel
$\boldsymbol{\tau}^s$	spanwise tangential vector of an aerodynamic panel
ρ	air density
$\boldsymbol{\Gamma}_b$	circulation strengths of bound vortices
$\dot{\boldsymbol{\Gamma}}_b$	changing rate of boundary circulation strengths
$\boldsymbol{\Gamma}_w$	circulation strengths of wake vortices
$\dot{\boldsymbol{\Gamma}}_w$	changing rate of wake circulation strengths
ζ_b	displacements of corner points in aerodynamic panels
$\dot{\zeta}_b$	velocities of corner points in aerodynamic panels
ζ_w	displacements of corner points in wake vortices
$\dot{\zeta}_w$	velocities of corner points in wake vortices

The unsteady vortex-lattice method (UVLM) is the most appropriate option for HALE vehicles, as a compromise between the computational cost and modeling fidelity. Although the DLM offers a faster way of computing unsteady aerodynamic loads, it is a linear method restricted to small out-of-plane harmonic motions with a flat wake. The UVLM is formulated in the time domain and features a free wake model that can capture the impact of wake vorticities on the distributed aerodynamic loads. Compared with CFD-based aerodynamic tools, the UVLM is more computationally economic and technically versatile when considering the nonlinear deformation and multidisciplinary coupling.

The UVLM roots in the foundation of the potential-flow vortex-lattice method (VLM), which is based on the concepts of vortex flows and circulation of vortices. The concept of vortex lattice was proposed and numerically simulated by Falkner in 1943 [15]. Hedman [16] established the classical steady VLM in 1965, dividing the lifting surface into small elements each containing a horseshoe vortex with its bound spanwise element along the swept quarter-chord of the element, and locating the collocation points for the non-penetration boundary condition at the three-quarter chord. The downwash at each collocation point was computed through the Biot-Savart law. Later on, the steady VLM continued to be improved and widely applied in many low-speed aerodynamic related studies [17–25]. The time-domain unsteady vortex-lattice method (UVLM) is the extension of VLM in non-stationary situations. Katz and Plotkin [26] gave a comprehensive description of this method. The UVLM has been applied in situations where free-wake modeling is necessary because of geometric complexity, such as flapping-wing kinematics, rotorcraft, or wind turbines. Recent papers also showed the capability of UVLM in dealing with problems like unsteady interference [27], computation of stability derivatives [28], flutter suppression [29], gust response [30], induced drag predictions [31], aero optimization [32], morphing vehicles [33–35], nonlinear aeroelasticity [36–38], and coupled aeroelasticity and flight dynamics [39–42]. Although the UVLM is seen as a computationally economic tool with medium fidelity, it can still be limited by computational power for large enough problems as the number of wake vortices keeps rising with time. To speed up the solution process, Hall [43] transformed the UVLM equations into discrete state-space form. Its dominant eigenvalues would define a reduced-order model to obtain the aeroelastic stability characteristics.

To facilitate using the UVLM in aeroelastic stability analysis and multidisciplinary optimization, aerodynamic sensitivities should be obtained firstly. While aerodynamic sensitivities of the steady VLM were studied several times, a sensitivity analysis of the UVLM with a free deforming wake model in the time domain was seldom carried out. Analytical sensitivities of the VLM were described by Chittick [44] and Stanford [45] in the context of optimizing coupled aeroelastic systems. Murthy [46] presented a semi-analytical method based on finite difference approximations for unsteady panel flows. The analytical sensitivities of the unsteady DLM in the frequency domain were also studied by Kolonay [47] and Li [48]. Stanford [49] studied the analytical sensitivity of the UVLM for flapping-wing optimization. The optimization problem aimed at maximizing propulsive efficiency under lift and thrust constraints. Therefore, his work mainly focused on the time history of overall lift and thrust sensitivities with respect to typical elastic modes of the flapping-wing.

Previous studies have provided good insights on the theoretical developments and practical applications of UVLM. However, there are few studies discussing the analytical aerodynamic sensitivity analysis with respect to both structural deformation and circulation strengths of vortices. This work gives a novel approach to obtain the analytical aerodynamic sensitivities based on the Chain Rules, for the purpose of formulating state-space aeroelastic equations with UVLM aerodynamics. First of all, a general description of the unsteady vortex lattice method is given, as well as the theoretical basis of a free wake shedding model. This is followed by detailed derivations of the analytical aerodynamic sensitivities, which emphasizes the handling technique for implicit functional relations. The section of numerical studies presents two time-domain aeroelastic analysis cases with different modeling fidelities. Sensitivity results are validated by the finite difference method, indicating that an effective analytical sensitivity calculation framework of UVLM is developed in this work.

2. Theoretical basis of the unsteady vortex-lattice method

The unsteady vortex-lattice method is described in the time domain. At the given time $t + 1$, the non-penetration boundary condition is satisfied at all collocation points, which can be expressed as

$$\mathbf{W}_{bb}^{t+1}\mathbf{\Gamma}_b^{t+1} + \mathbf{W}_{bw}^{t+1}\mathbf{\Gamma}_w^{t+1} = \mathbf{U}^{t+1} \cdot \mathbf{n} \tag{1}$$

where $\mathbf{\Gamma}_b$ and $\mathbf{\Gamma}_w$ are column vectors consisting of circulation strengths of bound and wake vortex panels, respectively. The matrix $\mathbf{W}_{bb}$ is formed by the influence coefficients of all bound vortex rings to all collocation points, while $\mathbf{W}_{bw}$ is the influence matrix of wake vortex rings to the collocation points. The left hand side of the equation is the total induced flow from the bound and wake vortices. On the right hand side, the column vector $\mathbf{U}$ consists of non-circulatory velocities, which are projected to the outward normal direction ($\mathbf{n}$) of the lifting surfaces. The non-circulatory velocities include contributions of aircraft rigid-body velocity, wing elastic vibration rate, and external air disturbance such as wind gust, if it exists. The entries of $\mathbf{W}_{bb}$ and $\mathbf{W}_{bw}$ are derived by using the Biot-Savart Law.

According to the Biot-Savart Law, every vortex segment of circulation Γ causes induced velocities for all spatial points. If the vortex segment points from a to b, the induced velocity at an arbitrary point p is obtained by

$$(\mathbf{q}_p)_{ab} = \frac{\Gamma}{4\pi}\mathbf{r}_0 \cdot \left(\frac{\mathbf{r}_1}{r_1} - \frac{\mathbf{r}_2}{r_2}\right)\frac{\mathbf{r}_1 \times \mathbf{r}_2}{|\mathbf{r}_1 \times \mathbf{r}_2|^2} \tag{2}$$

where

$$\mathbf{r}_0 = \mathbf{p}_b - \mathbf{p}_a$$
$$\mathbf{r}_1 = \mathbf{p} - \mathbf{p}_a$$
$$\mathbf{r}_2 = \mathbf{p} - \mathbf{p}_b$$

$\mathbf{r}_0$, $\mathbf{r}_1$ and $\mathbf{r}_2$ represent vectors of $\overline{ab}$, $\overline{ap}$ and $\overline{bp}$, respectively. Correspondingly, the influence of vortex segment $\overline{ab}$ at point p is obtained by assuming a unit vortex circulation strength, denoted as

$$\tilde{\mathbf{W}}_p\Big|_{ab} = \frac{1}{4\pi}\mathbf{r}_0 \cdot \left(\frac{\mathbf{r}_1}{r_1} - \frac{\mathbf{r}_2}{r_2}\right)\frac{\mathbf{r}_1 \times \mathbf{r}_2}{|\mathbf{r}_1 \times \mathbf{r}_2|^2} \tag{3}$$

Note that $\tilde{\mathbf{W}}_p$ is a vector, which is normal to the plane created by the point p and the vortex segment edge points a and b. This vector indicates the three-directional velocities induced by a vortex segment of the unit vortex circulation strength.

To calculate $\mathbf{W}_{bb}$, the influence of the jth vortex ring (with segments $\overline{ab}$, $\overline{bc}$, $\overline{cd}$ and $\overline{da}$, shown as Fig. 1) on collocation point i is obtained by the summation of contributions of each vortex segment, as

$$\left(\tilde{\mathbf{W}}_{bb}\right)_{ij} = \tilde{\mathbf{W}}_i\Big|_{ab} + \tilde{\mathbf{W}}_i\Big|_{bc} + \tilde{\mathbf{W}}_i\Big|_{cd} + \tilde{\mathbf{W}}_i\Big|_{da} \tag{4}$$

Additionally, $\left(\tilde{\mathbf{W}}_{bb}\right)_{ij}$ should be projected to the normal direction of vortex panel i (with segments $\overline{1234}$), resulting in

$$(\mathbf{W}_{bb})_{ij} = \left(\tilde{\mathbf{W}}_{bb}\right)_{ij} \cdot \mathbf{n}_i \tag{5}$$

where the normal vector of panel i is

$$\mathbf{n}_i = \frac{\mathbf{r}_{24} \times \mathbf{r}_{13}}{|\mathbf{r}_{24} \times \mathbf{r}_{13}|} \tag{6}$$

Both $\mathbf{r}_{24}$ and $\mathbf{r}_{13}$ are vectors defined by the positions of four corner points ($\mathbf{p}_1$, $\mathbf{p}_2$, $\mathbf{p}_3$, $\mathbf{p}_4$) of vortex panel i, as
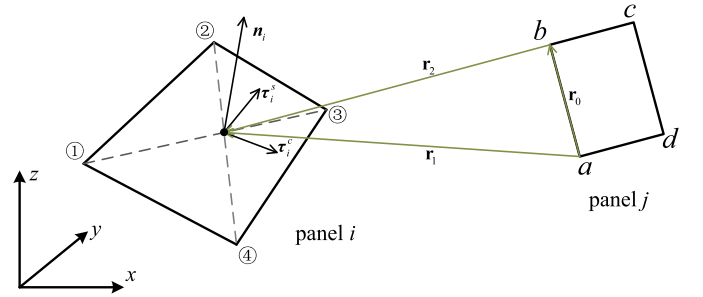

Fig. 1. Computation of the influence matrix between two vortex rings.

$$\mathbf{r}_{24} = \mathbf{p}_4 - \mathbf{p}_2$$
$$\mathbf{r}_{13} = \mathbf{p}_3 - \mathbf{p}_1$$

2.1. Aerodynamic loads

Aerodynamic forces are calculated from the unsteady Bernoulli equation. The pressure difference across each bound vortex panel acts along the panel's normal vector. According to Ref. [26], the pressure on each panel is

$$\Delta p_{m,n} = \rho\left[(\mathbf{U}_{m,n} + \mathbf{u}_{m,n}^w)\left(\boldsymbol{\tau}_{m,n}^c\frac{\Gamma_{m,n} - \Gamma_{m-1,n}}{c_{m,n}}\right.\right.$$
$$\left.\left. + \boldsymbol{\tau}_{m,n}^s\frac{\Gamma_{m,n} - \Gamma_{m,n-1}}{b_{m,n}}\right) + \dot{\Gamma}_{m,n}\right] \tag{7}$$

where $\mathbf{U}$ is the complete non-circulatory velocity consists of aircraft rigid-body velocity, wing vibration, wind gust, etc. The air density is symbolized as ρ. The spanwise index m and chordwise index n are used to locate the very panel considered. $b_{m,n}$ and $c_{m,n}$ are span length and chord length, respectively. Γ represents the circulation strength of current vortex panel. $\mathbf{u}^w$ is the wake induced velocity at each control point, which can be obtained from the influence matrix $\tilde{\mathbf{W}}_{bw}$ and circulation strengths of wake vortices $\mathbf{\Gamma}_w$, as

$$\mathbf{u}^w = \tilde{\mathbf{W}}_{bw}\mathbf{\Gamma}_w \tag{8}$$

and $\boldsymbol{\tau}^c$ and $\boldsymbol{\tau}^s$ are the tangential vectors of the panel in the chordwise and spanwise directions, respectively. The normal force acting on the panel is then

$$\mathbf{F}_{m,n} = \left(\Delta p_{m,n}b_{m,n}c_{m,n}\right)\mathbf{n}_{m,n} \tag{9}$$

However, due to the fact that lifting-surface methods such as the UVLM are based on thin-wing approximation, the aerodynamic loads derived here do not account for the leading-edge suction effect. Only the component normal to the non-circulatory velocity is retained, i.e., the contribution of pressure to the local lift. This is done by finding the angle of attack of the panel $\alpha_{m,n}$ with respect to the non-circulatory velocity, as

$$L_{m,n} = \rho b_{m,n}c_{m,n}\cos\alpha_{m,n}\left[(\mathbf{U}_{m,n} + \mathbf{u}_{m,n}^w) \cdot \boldsymbol{\tau}_{m,n}^c\frac{\Gamma_{m,n} - \Gamma_{m-1,n}}{c_{m,n}}\right.$$
$$\left. + (\mathbf{U}_{m,n} + \mathbf{u}_{m,n}^w) \cdot \boldsymbol{\tau}_{m,n}^s\frac{\Gamma_{m,n} - \Gamma_{m,n-1}}{b_{m,n}} + \dot{\Gamma}_{m,n}\right] \tag{10}$$

Similarly, according to Ref. [26], the induced drag on each panel $D_{m,n}$ can be expressed as

$$D_{m,n} = \rho\left[(w_{m,n}^b + w_{m,n}^w)(\Gamma_{m,n} - \Gamma_{m-1,n})b_{m,n}\right.$$
$$\left. + \dot{\Gamma}_{m,n}b_{m,n}c_{m,n}\sin\alpha_{m,n}\right] \tag{11}$$

where w^b is the (normal) downwash induced by the wing's streamwise vortex segments. w^w is the vertical component of the all wake induced velocity.

Both Eq. (10) and Eq. (11) can be transformed into matrix forms. For instance, the lift formulation is then given as

$$\mathbf{L} = \rho \mathbf{G}_1 (\mathbf{U}_1 \mathbf{E}_1 \Gamma + \mathbf{U}_2 \mathbf{E}_2 \Gamma + \dot{\Gamma}) \tag{12}$$

Where $\mathbf{E}_1$ and $\mathbf{E}_2$ are sparse matrices filled with 1 and -1 in the correct positions in order to account for adjacent panels; $\mathbf{G}_1 = f(\zeta_b, \dot{\zeta}_b)$ is a matrix dependent on the panel geometry and local angle of incidence; $\mathbf{U}_{1(2)} = f(\zeta_b, \dot{\zeta}_b, \zeta_w, \Gamma_w)$ are diagonal matrices that store weighted velocities. Their exact definition can be given as follows,

$$\mathbf{G}_1 = \begin{bmatrix} \ddots & & \\ & b_k c_k \cos \alpha_k & \\ & & \ddots \end{bmatrix} \tag{13}$$

$$\mathbf{U}_1 = \begin{bmatrix} \ddots & & \\ & \frac{(\mathbf{U}_k + \mathbf{u}_k^w) \boldsymbol{\tau}_k^c}{c_k} & \\ & & \ddots \end{bmatrix} \tag{14}$$

$$\mathbf{U}_2 = \begin{bmatrix} \ddots & & \\ & \frac{(\mathbf{U}_k + \mathbf{u}_k^w) \boldsymbol{\tau}_k^s}{b_k} & \\ & & \ddots \end{bmatrix} \tag{15}$$

According to Eq. (8), the wake induced velocity $\mathbf{u}_k^w$ is determined by wake circulation strengths Γ_w, thus $\mathbf{U}_1$ and $\mathbf{U}_2$ can be rewritten as

$$\mathbf{U}_1 = diag \left\{ \frac{\mathbf{U} \boldsymbol{\tau}^c + \mathbf{W}_{bw}^c \Gamma_b}{c_k} \right\} \tag{16}$$

$$\mathbf{U}_2 = diag \left\{ \frac{\mathbf{U} \boldsymbol{\tau}^s + \mathbf{W}_{bw}^s \Gamma_b}{b_k} \right\} \tag{17}$$

The angle of attack α_k is found by resolving vector $\mathbf{U}_k$ along the chord (tangent) and outward normal of panel k and then using an arctangent function

$$\alpha_k = \tan^{-1} \left(\frac{-\mathbf{U}_k \cdot \mathbf{n}_k}{\mathbf{U}_k \cdot \boldsymbol{\tau}_k^c} \right) = \tan^{-1} \frac{-U_k^n}{U_k^c} \tag{18}$$

Similarly, the drag is written as

$$\mathbf{D} = \rho \left(\mathbf{U}_3 \mathbf{E}_1 \Gamma_b + \mathbf{G}_2 \dot{\Gamma}_b \right) \tag{19}$$

where $\mathbf{G}_2$ is a matrix dependent on the panel geometry and angle of incidence, similar to $\mathbf{G}_1$. $\mathbf{U}_3$ is a diagonal matrix that stores weighted velocities in all bound vortex panels, similar to $\mathbf{U}_1$ and $\mathbf{U}_2$. They are denoted as

$$\mathbf{G}_2 = \begin{bmatrix} \ddots & & \\ & b_k c_k \sin \alpha_k & \\ & & \ddots \end{bmatrix} \tag{20}$$

$$\mathbf{U}_3 = \begin{bmatrix} \ddots & & \\ & \left(w^b + w^w \right)_k b_k & \\ & & \ddots \end{bmatrix} \tag{21}$$

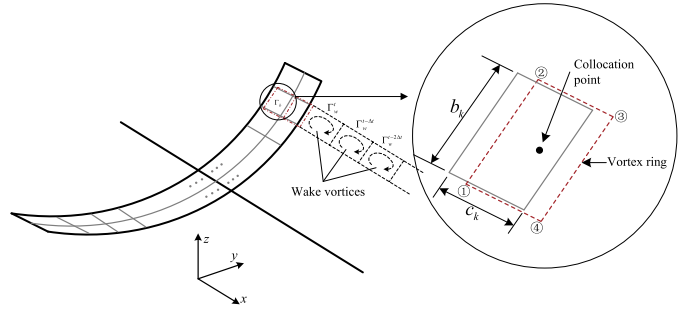The downwash components are calculated using similar influence matrices, as

Fig. 2. Boundary vortex rings on the lifting surface and the free wake model.

$$\mathbf{w}^b + \mathbf{w}^w = \bar{\mathbf{W}}_{bb} \Gamma_b + \bar{\mathbf{W}}_{bw} \Gamma_w \tag{22}$$

where $\bar{\mathbf{W}}_{bb}$ is obtained in a similar way as $\mathbf{W}_{bb}$, yet it should only account for the streamwise vortex segments plus the trailing edge of the surface. It is also projected along the normal of each panel.

2.2. Free wake model

A free wake model is necessary for accurate unsteady aerodynamics and is implemented in the current study. At each time step, one row of new vortex rings shed from the wing trailing edge (as shown in Fig. 2), with the circulation strength equivalent to the original bound vorticity at the trailing edge. At the same time, the existing wake rings convect according to the local velocity field, preserving their circulation strengths. Therefore, the wake circulation propagates in the discrete time domain according to the following equation

$$\Gamma_w^{t+1} = \mathbf{A}_b^t \Gamma_b^t + \mathbf{A}_w^t \Gamma_w^t \tag{23}$$

which gives the wake circulation Γ_w in Eq. (1) according to the previous time solution. $\mathbf{A}_b$ and $\mathbf{A}_w$ are both sparse matrices, given as

$$\mathbf{A}_b = \begin{bmatrix} \mathbf{0} & \cdots & \mathbf{0} & \cdots & \mathbf{I} \\ \vdots & \ddots & \vdots & \vdots & \vdots \\ \mathbf{0} & \cdots & \mathbf{0} & \cdots & \mathbf{0} \\ \vdots & \vdots & \vdots & \ddots & \vdots \\ \mathbf{0} & \cdots & \mathbf{0} & \cdots & \mathbf{0} \end{bmatrix} \tag{24}$$

and each block of $\mathbf{A}_b$ is either a zero or an identity matrix with a dimension of m. While the dimension of Γ_b is fixed, the total dimension of $\mathbf{A}_b \Gamma_b$ is same as Γ_w. Therefore, the row number of $\mathbf{A}_b$ changes with time and equals to the total number of wake vortices. $\mathbf{A}_b$ represents the shedding mechanism of bound vorticities at the trailing edge of the wing. The second propagation matrix for wake circulations is formed in a similar way, which is given as

$$\mathbf{A}_w = \begin{bmatrix} \mathbf{0} & \mathbf{0} & \cdots & \mathbf{0} & \mathbf{0} \\ \mathbf{I} & \mathbf{0} & \cdots & \mathbf{0} & \mathbf{0} \\ \mathbf{0} & \mathbf{I} & \cdots & \mathbf{0} & \mathbf{0} \\ \vdots & \vdots & \ddots & \vdots & \vdots \\ \mathbf{0} & \mathbf{0} & \cdots & \mathbf{I} & \mathbf{0} \end{bmatrix} \tag{25}$$

each block of $\mathbf{A}_w$ is still a $(m \times m)$ matrix. $\mathbf{A}_w$ represents the position changing of the previous wake vorticities in one time step.

The newly formed wake includes a row of grids located at the trailing edge of bound vortex panels and all existing wake grids. The velocity vector of all wake grid points $\mathbf{v}_w$ is determined by

$$\mathbf{v}_w^t = \tilde{\mathbf{W}}_{wb}^t \Gamma_b^t + \tilde{\mathbf{W}}_{ww}^t \Gamma_w^t + \mathbf{v}_d \tag{26}$$

which is analogous to the non-penetration boundary condition. However, the velocities in this case are not projected along any vector, with all three components retained. $\tilde{\mathbf{W}}_{wb}$ and $\tilde{\mathbf{W}}_{ww}$ are bound-to-wake and wake-to-wake influence matrices, respectively. $\mathbf{v}_d$ represents contribution from external disturbance.

Meanwhile, the locations of all the previous wake grid points at the new time step $\bar{\zeta}_w^{t+1}$ is calculated by

$$\bar{\zeta}_w^{t+1} = \zeta_w^t + \mathbf{v}_w^t \Delta t \tag{27}$$

which indicates the previous wake grids moving with their local velocities $\mathbf{v}_w$ in one time step Δt.

As a result, the coordinates of all wake grid points at the new time step are written as

$$\zeta_w^{t+1} = \mathbf{B}_b^t \zeta_b^{t+1} + \mathbf{B}_w^t \bar{\zeta}_w^{t+1} \tag{28}$$

Note that ζ_b is evaluated at the new time step, which is updated by the elastic solver. If $\mathbf{v}_w$ is set as zero, the wake model is then reduced to a prescribed one, which also eliminates Eq. (26). Similar to the circulation propagation matrices, the propagation matrices for panel points, $\mathbf{B}_b$ and $\mathbf{B}_w$, are both sparse matrices, given as

$$\mathbf{B}_b = \begin{bmatrix} \mathbf{0} & \cdots & \mathbf{0} & \cdots & \mathbf{I} \\ \vdots & \ddots & \vdots & \vdots & \vdots \\ \mathbf{0} & \cdots & \mathbf{0} & \cdots & \mathbf{0} \\ \vdots & \vdots & \vdots & \ddots & \vdots \\ \mathbf{0} & \cdots & \mathbf{0} & \cdots & \mathbf{0} \end{bmatrix}, \quad \mathbf{B}_w = \begin{bmatrix} \mathbf{0} & \mathbf{0} & \cdots & \mathbf{0} & \mathbf{0} \\ \mathbf{I} & \mathbf{0} & \cdots & \mathbf{0} & \mathbf{0} \\ \mathbf{0} & \mathbf{I} & \cdots & \mathbf{0} & \mathbf{0} \\ \vdots & \vdots & \ddots & \vdots & \vdots \\ \mathbf{0} & \mathbf{0} & \cdots & \mathbf{I} & \mathbf{0} \end{bmatrix} \tag{29}$$

$\mathbf{B}_b$ extracts the coordinates of bound corner points at the trailing edge of the wing, which forms the new first row of wake grid points. $\mathbf{B}_w$ adjusts the previous wake grid points to new locations in matrix ζ_w. The dimensions of both $\mathbf{B}_b$ and $\mathbf{B}_w$ increase with time, as new wake panels are generated at each time step.

3. Analytical sensitivity analysis framework

The typical aeroelastic equation of motion can be written as

$$\mathbf{M} \begin{Bmatrix} \ddot{\mathbf{x}} \\ \ddot{\mathbf{y}} \\ \ddot{\mathbf{z}} \end{Bmatrix} + \mathbf{C} \begin{Bmatrix} \dot{\mathbf{x}} \\ \dot{\mathbf{y}} \\ \dot{\mathbf{z}} \end{Bmatrix} + \mathbf{K} \begin{Bmatrix} \mathbf{x} \\ \mathbf{y} \\ \mathbf{z} \end{Bmatrix} = \begin{Bmatrix} \mathbf{F}_x \\ \mathbf{F}_y \\ \mathbf{F}_z \end{Bmatrix} \tag{30}$$

Where $\mathbf{M}$, $\mathbf{K}$, $\mathbf{C}$ are the structural mass, damping and stiffness matrix, respectively. Matrix $\mathbf{F}$ represents the aerodynamic loads including lift $\mathbf{L}$ and drag $\mathbf{D}$. Vectors $\mathbf{x}$, $\mathbf{y}$ and $\mathbf{z}$ are global coordinates of structural nodes. For simplicity, only lift is considered in the following derivation for aerodynamic sensitivity.

Perform a small perturbation on the aeroelastic equation of motion Eq. (30), it yields to

$$\mathbf{M} \begin{Bmatrix} \ddot{\mathbf{x}}_0 + \Delta \ddot{\mathbf{x}} \\ \ddot{\mathbf{y}}_0 + \Delta \ddot{\mathbf{y}} \\ \ddot{\mathbf{z}}_0 + \Delta \ddot{\mathbf{z}} \end{Bmatrix} + \mathbf{C} \begin{Bmatrix} \dot{\mathbf{x}}_0 + \Delta \dot{\mathbf{x}} \\ \dot{\mathbf{y}}_0 + \Delta \dot{\mathbf{y}} \\ \dot{\mathbf{z}}_0 + \Delta \dot{\mathbf{z}} \end{Bmatrix} + \mathbf{K} \begin{Bmatrix} \mathbf{x}_0 + \Delta \mathbf{x} \\ \mathbf{y}_0 + \Delta \mathbf{y} \\ \mathbf{z}_0 + \Delta \mathbf{z} \end{Bmatrix}$$
$$= \begin{Bmatrix} \mathbf{L}_{x0} + \frac{\partial \mathbf{L}_x}{\partial \zeta_b} \Delta \zeta_b + \frac{\partial \mathbf{L}_x}{\partial \dot{\zeta}_b} \Delta \dot{\zeta}_b + \frac{\partial \mathbf{L}_x}{\partial \mathbf{\Gamma}_b} \Delta \mathbf{\Gamma}_b + \frac{\partial \mathbf{L}_x}{\partial \mathbf{\Gamma}_w} \Delta \mathbf{\Gamma}_w + \frac{\partial \mathbf{L}_x}{\partial \dot{\mathbf{\Gamma}}_b} \Delta \dot{\mathbf{\Gamma}}_b \\ \mathbf{L}_{y0} + \frac{\partial \mathbf{L}_y}{\partial \zeta_b} \Delta \zeta_b + \frac{\partial \mathbf{L}_y}{\partial \dot{\zeta}_b} \Delta \dot{\zeta}_b + \frac{\partial \mathbf{L}_y}{\partial \mathbf{\Gamma}_b} \Delta \mathbf{\Gamma}_b + \frac{\partial \mathbf{L}_y}{\partial \mathbf{\Gamma}_w} \Delta \mathbf{\Gamma}_w + \frac{\partial \mathbf{L}_y}{\partial \dot{\mathbf{\Gamma}}_b} \Delta \dot{\mathbf{\Gamma}}_b \\ \mathbf{L}_{z0} + \frac{\partial \mathbf{L}_z}{\partial \zeta_b} \Delta \zeta_b + \frac{\partial \mathbf{L}_z}{\partial \dot{\zeta}_b} \Delta \dot{\zeta}_b + \frac{\partial \mathbf{L}_z}{\partial \mathbf{\Gamma}_b} \Delta \mathbf{\Gamma}_b + \frac{\partial \mathbf{L}_z}{\partial \mathbf{\Gamma}_w} \Delta \mathbf{\Gamma}_w + \frac{\partial \mathbf{L}_z}{\partial \dot{\mathbf{\Gamma}}_b} \Delta \dot{\mathbf{\Gamma}}_b \end{Bmatrix} \tag{31}$$

Cross all terms with zero subscript out in Eq. (31), the perturbed aeroelastic equation of motion becomes
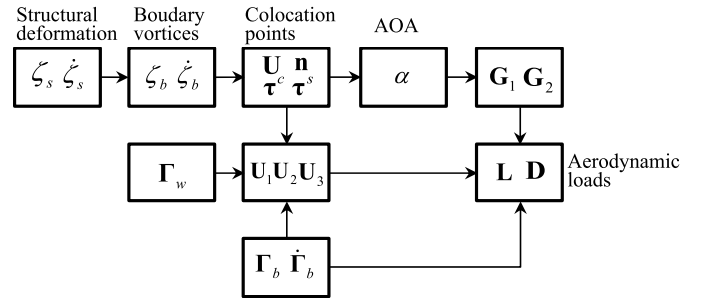

Fig. 3. The relations between aerodynamic loads and structural deformation variables.

$$\mathbf{M} \begin{Bmatrix} \Delta \ddot{\mathbf{x}} \\ \Delta \ddot{\mathbf{y}} \\ \Delta \ddot{\mathbf{z}} \end{Bmatrix} + \mathbf{C} \begin{Bmatrix} \Delta \dot{\mathbf{x}} \\ \Delta \dot{\mathbf{y}} \\ \Delta \dot{\mathbf{z}} \end{Bmatrix} + \mathbf{K} \begin{Bmatrix} \Delta \mathbf{x} \\ \Delta \mathbf{y} \\ \Delta \mathbf{z} \end{Bmatrix}$$
$$= \begin{Bmatrix} \frac{\partial \mathbf{L}_x}{\partial \zeta_b} \Delta \zeta_b + \frac{\partial \mathbf{L}_x}{\partial \dot{\zeta}_b} \Delta \dot{\zeta}_b + \frac{\partial \mathbf{L}_x}{\partial \mathbf{\Gamma}_b} \Delta \mathbf{\Gamma}_b + \frac{\partial \mathbf{L}_x}{\partial \mathbf{\Gamma}_w} \Delta \mathbf{\Gamma}_w + \frac{\partial \mathbf{L}_x}{\partial \dot{\mathbf{\Gamma}}_b} \Delta \dot{\mathbf{\Gamma}}_b \\ \frac{\partial \mathbf{L}_y}{\partial \zeta_b} \Delta \zeta_b + \frac{\partial \mathbf{L}_y}{\partial \dot{\zeta}_b} \Delta \dot{\zeta}_b + \frac{\partial \mathbf{L}_y}{\partial \mathbf{\Gamma}_b} \Delta \mathbf{\Gamma}_b + \frac{\partial \mathbf{L}_y}{\partial \mathbf{\Gamma}_w} \Delta \mathbf{\Gamma}_w + \frac{\partial \mathbf{L}_y}{\partial \dot{\mathbf{\Gamma}}_b} \Delta \dot{\mathbf{\Gamma}}_b \\ \frac{\partial \mathbf{L}_z}{\partial \zeta_b} \Delta \zeta_b + \frac{\partial \mathbf{L}_z}{\partial \dot{\zeta}_b} \Delta \dot{\zeta}_b + \frac{\partial \mathbf{L}_z}{\partial \mathbf{\Gamma}_b} \Delta \mathbf{\Gamma}_b + \frac{\partial \mathbf{L}_z}{\partial \mathbf{\Gamma}_w} \Delta \mathbf{\Gamma}_w + \frac{\partial \mathbf{L}_z}{\partial \dot{\mathbf{\Gamma}}_b} \Delta \dot{\mathbf{\Gamma}}_b \end{Bmatrix} \tag{32}$$

It is noticed that the motions of aerodynamic corner points (ζ_b and $\dot{\zeta}_b$) are mapped from structural motions ($\mathbf{x}$, $\mathbf{y}$, $\mathbf{z}$ and $\dot{\mathbf{x}}$, $\dot{\mathbf{y}}$, $\dot{\mathbf{z}}$). Thus all terms of ζ_b and $\dot{\zeta}_b$ can be transferred to the left side of Eq. (32) and merged into structural motions. Therefore the perturbed aeroelastic equation of motion can be denoted as

$$\bar{\mathbf{M}} \begin{Bmatrix} \Delta \ddot{\mathbf{x}} \\ \Delta \ddot{\mathbf{y}} \\ \Delta \ddot{\mathbf{z}} \end{Bmatrix} + \bar{\mathbf{C}} \begin{Bmatrix} \Delta \dot{\mathbf{x}} \\ \Delta \dot{\mathbf{y}} \\ \Delta \dot{\mathbf{z}} \end{Bmatrix} + \bar{\mathbf{K}} \begin{Bmatrix} \Delta \mathbf{x} \\ \Delta \mathbf{y} \\ \Delta \mathbf{z} \end{Bmatrix}$$
$$= \frac{\partial \mathbf{L}}{\partial \mathbf{\Gamma}_b} \Delta \mathbf{\Gamma}_b + \frac{\partial \mathbf{L}}{\partial \mathbf{\Gamma}_w} \Delta \mathbf{\Gamma}_w + \frac{\partial \mathbf{L}}{\partial \dot{\mathbf{\Gamma}}_b} \Delta \dot{\mathbf{\Gamma}}_b \tag{33}$$

As stated in Ref. [42], the linearization of the nonlinear aerodynamic model should be implemented to simplify the procedure of incorporating the UVLM with aeroelastic equations. The linearization is based on the assumption that the structural deformation around the equilibrium condition is small. Therefore, in calculations of the wing-to-wing, wake-to-wing influence matrices $\mathbf{W}_{bb}$ and $\mathbf{W}_{bw}$, both structural geometry and wake geometry are seen frozen as the reference condition. That is, the dependencies on ζ_b and ζ_w is ignored for $\mathbf{W}_{bb}$ and $\mathbf{W}_{bw}$ in Eq. (1).

However, the orientation and magnitude of aerodynamic loads are still dependent on ζ_b and $\dot{\zeta}_b$. The deformed lifting surface determines the local angle of incidence and local velocity at the collocation point. Then matrices $\mathbf{G}_{1(2)}$, $\mathbf{U}_{1(2)(3)}$ are affected by ζ_b and $\dot{\zeta}_b$ based on the functional relations described in Eq. (13)~(21). Matrices $\mathbf{G}_{1(2)}$, $\mathbf{U}_{1(2)(3)}$ finally determine the aerodynamic loads based on Eq. (12). As a result, the analytical sensitivities of aerodynamic loads with respect to ζ_b and $\dot{\zeta}_b$ are emphasized in the following sections, and once they are obtained, Eq. (32) can be transferred to Eq. (33) to establish the linearized aeroelastic equation of motion around the equilibrium condition.

Fig. 3 shows the detailed variable relations in the derivation of UVLM aerodynamics. The linearization neglects the impacts of ζ_b and ζ_w on the influence matrices.

Using a mid-point integration scheme for the derivatives of the bound circulations, and performing a small perturbation analysis on the general UVLM equations, the incremental propagation equations are obtained as

$$\mathbf{W}_{bb}^0 \Delta \mathbf{\Gamma}_b^{t+1} + \mathbf{W}_{bw}^0 \Delta \mathbf{\Gamma}_w^{t+1} = (\frac{\partial \mathbf{U}}{\partial \zeta_b})^0 \Delta \zeta_b^{t+1} + (\frac{\partial \mathbf{U}}{\partial \dot{\zeta}_b})^0 \Delta \dot{\zeta}_b^{t+1}$$

$$\Delta \mathbf{\Gamma}_w^{t+1} = \mathbf{A}_b^0 \Delta \mathbf{\Gamma}_b^t + \mathbf{A}_w^0 \Delta \mathbf{\Gamma}_w^t \qquad (34)$$

$$\frac{\Delta \mathbf{\Gamma}_b^{t+1} - \Delta \mathbf{\Gamma}_b^t}{\Delta t} = \frac{1}{2}(\Delta \dot{\mathbf{\Gamma}}_b^{t+1} + \Delta \dot{\mathbf{\Gamma}}_b^t)$$

where Δt is the time step increment, and the superscript 0 represents the reference condition where the linearization take place. Combine the perturbed aeroelastic equation Eq. (33) with the incremental propagation equations Eq. (34), the discrete-time-state-space aeroelastic equation can be finally obtained,

$$\begin{Bmatrix} \mathbf{X}_s^{n+1} \\ \dot{\mathbf{X}}_s^{n+1} \\ \mathbf{\Gamma}_b^{n+1} \\ \mathbf{\Gamma}_w^{n+1} \\ \dot{\mathbf{\Gamma}}_b^{N+1} \end{Bmatrix} = \begin{bmatrix} & & \mathbf{H} & & \end{bmatrix} \begin{Bmatrix} \mathbf{X}_s^{n} \\ \dot{\mathbf{X}}_s^{n} \\ \mathbf{\Gamma}_b^{n} \\ \mathbf{\Gamma}_w^{n} \\ \dot{\mathbf{\Gamma}}_b^{n} \end{Bmatrix} \qquad (35)$$

where

$$\mathbf{X}_s = \{\mathbf{x}, \mathbf{y}, \mathbf{z}\}^T, \qquad \zeta_b = \mathbf{T} \cdot \mathbf{X}_s, \qquad \dot{\zeta}_b = \mathbf{T} \cdot \dot{\mathbf{X}}_s$$

$\mathbf{X}_s$ and $\dot{\mathbf{X}}_s$ are matrices of structural displacement and velocity, respectively. $\mathbf{T}$ is the transfer matrix from structural grids to aerodynamic grids. $\mathbf{H}$ is the system matrix which includes several unknown sensitivity terms. These terms are $\frac{\partial \mathbf{L}}{\partial \zeta_b}$, $\frac{\partial \mathbf{L}}{\partial \dot{\zeta}_b}$, $\frac{\partial \mathbf{L}}{\partial \mathbf{\Gamma}_b}$, $\frac{\partial \mathbf{L}}{\partial \mathbf{\Gamma}_w}$, and $\frac{\partial \mathbf{L}}{\partial \dot{\mathbf{\Gamma}}_b}$. Once these sensitivity terms are calculated, the aeroelastic equation in a state-space form and its system matrix $\mathbf{H}$ can be easily obtained.

By using the chain rule, the analytical aerodynamic lift sensitivities can be derived based on the relations described in Fig. 3, as

$$\frac{\partial \mathbf{L}}{\partial \zeta_b} = \frac{\partial \mathbf{L}}{\partial \mathbf{G}_1} \cdot \frac{\partial \mathbf{G}_1}{\partial \zeta_b} + \frac{\partial \mathbf{L}}{\partial \mathbf{U}_1} \cdot \frac{\partial \mathbf{U}_1}{\partial \zeta_b} + \frac{\partial \mathbf{L}}{\partial \mathbf{U}_2} \cdot \frac{\partial \mathbf{U}_2}{\partial \zeta_b}$$

$$\frac{\partial \mathbf{L}}{\partial \dot{\zeta}_b} = \frac{\partial \mathbf{L}}{\partial \mathbf{G}_1} \cdot \frac{\partial \mathbf{G}_1}{\partial \dot{\zeta}_b} + \frac{\partial \mathbf{L}}{\partial \mathbf{U}_1} \cdot \frac{\partial \mathbf{U}_1}{\partial \dot{\zeta}_b} + \frac{\partial \mathbf{L}}{\partial \mathbf{U}_2} \cdot \frac{\partial \mathbf{U}_2}{\partial \dot{\zeta}_b}$$

$$\frac{\partial \mathbf{L}}{\partial \mathbf{\Gamma}_b} = \rho \mathbf{G}_1(\mathbf{U}_1 \mathbf{E}_1 + \mathbf{U}_2 \mathbf{E}_2) \qquad (36)$$

$$\frac{\partial \mathbf{L}}{\partial \mathbf{\Gamma}_w} = \frac{\partial \mathbf{L}}{\partial \mathbf{U}_1} \cdot \frac{\partial \mathbf{U}_1}{\partial \mathbf{\Gamma}_w} + \frac{\partial \mathbf{L}}{\partial \mathbf{U}_2} \cdot \frac{\partial \mathbf{U}_2}{\partial \mathbf{\Gamma}_w}$$

$$\frac{\partial \mathbf{L}}{\partial \dot{\mathbf{\Gamma}}_b} = \rho \mathbf{G}_1$$

In Eq. (36), sensitivity terms $\frac{\partial \mathbf{L}}{\partial \zeta_b}$ and $\frac{\partial \mathbf{L}}{\partial \dot{\zeta}_b}$ represent the impact of structural motions on the aerodynamic loads distributed on bound vortex panels. Sensitivity terms $\frac{\partial \mathbf{L}}{\partial \mathbf{\Gamma}_b}$, $\frac{\partial \mathbf{L}}{\partial \mathbf{\Gamma}_w}$ and $\frac{\partial \mathbf{L}}{\partial \dot{\mathbf{\Gamma}}_b}$ represent the impact of both bound and wake vorticities on the distributed aerodynamic loads. It is straightforward to compute terms like $\frac{\partial \mathbf{L}}{\partial \mathbf{G}_1}$, $\frac{\partial \mathbf{L}}{\partial \mathbf{U}_1}$ and $\frac{\partial \mathbf{L}}{\partial \mathbf{U}_2}$ base on Eq. (12). However, terms like $\frac{\partial \mathbf{G}_1}{\partial \zeta_b}$, $\frac{\partial \mathbf{G}_1}{\partial \dot{\zeta}_b}$ and $\frac{\partial \mathbf{U}_1}{\partial \zeta_b}$ are not so easy to obtain, as ζ_b $\dot{\zeta}_b$ are contained implicitly in vectors $\mathbf{n}$ and $\mathbf{\tau}$, or the angle of attack α. The relations of variables including ζ_b, $\dot{\zeta}_b$, $\mathbf{\Gamma}_b$ and $\mathbf{\Gamma}_w$ are described in Fig. 3.

Take $\frac{\partial \mathbf{G}_1}{\partial \zeta_{1x}}$ for example,

$$\frac{\partial \mathbf{G}_1}{\partial \zeta_{1x}} = \frac{\partial \mathbf{G}_1}{\partial \cos \alpha} \cdot \frac{\partial \cos \alpha}{\partial \alpha} \cdot \frac{\partial \alpha}{\partial \frac{U^n}{U^c}} \cdot \frac{\partial \frac{U^n}{U^c}}{\partial \zeta_{1x}}$$

$$= b_k c_k (-\sin \alpha_k) \left(\frac{1}{1 + (\frac{U^n}{U^c})^2} \right) \qquad (37)$$

$$\cdot \left(\frac{\partial \frac{U^n}{U^c}}{\partial \tau_x} \frac{\partial \tau_x}{\partial \zeta_{1x}} + \frac{\partial \frac{U^n}{U^c}}{\partial n_y} \frac{\partial n_y}{\partial \zeta_{1x}} + \frac{\partial \frac{U^n}{U^c}}{\partial n_z} \frac{\partial n_z}{\partial \zeta_{1x}} \right)$$

where U^c and U^n are tangential and normal velocity of the collocation point, respectively. The chordwise tangential vector $\mathbf{\tau}^c = (\tau_1, \tau_2, \tau_3)$ and normal vector $\mathbf{n} = (n_1, n_2, n_3)$ at the collocation point can be calculated approximately using the displacements of four corner points in a panel ($\zeta_1, \zeta_2, \zeta_3, \zeta_4$), as Eq. (38) and Eq. (39) show:

$$\tau_1 = \frac{\tau_x}{\sqrt{\tau_x^2 + \tau_y^2 + \tau_z^2}} = \frac{\zeta_{3x} + \zeta_{4x} - \zeta_{1x} - \zeta_{2x}}{2} / \sqrt{\tau_x^2 + \tau_y^2 + \tau_z^2}$$

$$\tau_2 = \frac{\tau_y}{\sqrt{\tau_x^2 + \tau_y^2 + \tau_z^2}} = \frac{\zeta_{3y} + \zeta_{4y} - \zeta_{1y} - \zeta_{2y}}{2} / \sqrt{\tau_x^2 + \tau_y^2 + \tau_z^2}$$

$$\tau_3 = \frac{\tau_z}{\sqrt{\tau_x^2 + \tau_y^2 + \tau_z^2}} = \frac{\zeta_{3z} + \zeta_{4z} - \zeta_{1z} - \zeta_{2z}}{2} / \sqrt{\tau_x^2 + \tau_y^2 + \tau_z^2}$$

$$(38)$$

$$n_1 = \frac{n_x}{\sqrt{n_x^2 + n_y^2 + n_z^2}}$$
$$= \frac{(\zeta_{4y} - \zeta_{2y})(\zeta_{3z} - \zeta_{1z}) - (\zeta_{3y} - \zeta_{1y})(\zeta_{4z} - \zeta_{2z})}{\sqrt{n_x^2 + n_y^2 + n_z^2}}$$

$$n_2 = \frac{n_y}{\sqrt{n_x^2 + n_y^2 + n_z^2}}$$
$$= \frac{(\zeta_{3x} - \zeta_{1x})(\zeta_{4z} - \zeta_{2z}) - (\zeta_{4x} - \zeta_{2x})(\zeta_{3z} - \zeta_{1z})}{\sqrt{n_x^2 + n_y^2 + n_z^2}} \qquad (39)$$

$$n_3 = \frac{n_z}{\sqrt{n_x^2 + n_y^2 + n_z^2}}$$
$$= \frac{(\zeta_{4x} - \zeta_{2x})(\zeta_{3y} - \zeta_{1y}) - (\zeta_{3x} - \zeta_{1x})(\zeta_{4y} - \zeta_{2y})}{\sqrt{n_x^2 + n_y^2 + n_z^2}}$$

Thus, every partial derivative term in $\frac{\partial \mathbf{G}_1}{\partial \zeta_{1x}}$ of Eq. (37) can be derived as

$$\frac{\partial \frac{U^n}{U^c}}{\partial \tau_x} = \frac{\partial \left(\frac{U_x n_1 + U_y n_2 + U_z n_3}{U_x \tau_1 + U_y \tau_2 + U_z \tau_3} \right)}{\partial \tau_x} = U^n \cdot \frac{\partial \frac{1}{U^c}}{\partial U^c} \cdot \frac{\partial U^c}{\partial \tau_x} \qquad (40)$$

$$= -U^n \cdot \frac{1}{(U^c)^2} \cdot \left(U_x \frac{\partial \tau_1}{\partial \tau_x} + U_y \frac{\partial \tau_2}{\partial \tau_x} + U_z \frac{\partial \tau_3}{\partial \tau_x} \right)$$

$$= -U^n \cdot \frac{1}{(U^c)^2} \cdot \left[U_x(\tau_y^2 + \tau_z^2) - U_y \tau_x \tau_y - U_z \tau_x \tau_z \right]$$

$$\cdot (\tau_x^2 + \tau_y^2 + \tau_z^2)^{-\frac{3}{2}}$$

$$\frac{\partial \tau_x}{\partial \zeta_{1x}} = \frac{\partial \left(\frac{\zeta_{3x} + \zeta_{4x} - \zeta_{1x} - \zeta_{2x}}{2} \right)}{\partial \zeta_{1x}} = -\frac{1}{2} \qquad (41)$$

$$\frac{\partial \frac{U^n}{U^c}}{\partial n_y} = \frac{\partial \left(\frac{U_x n_1 + U_y n_2 + U_z n_3}{U_x \tau_1 + U_y \tau_2 + U_z \tau_3} \right)}{\partial n_y} \qquad (42)$$

$$= \frac{1}{U^c} \left(U_x \frac{\partial n_1}{\partial n_y} + U_y \frac{\partial n_2}{\partial n_y} + U_z \frac{\partial n_3}{\partial n_y} \right)$$

$$= \frac{1}{U^c} \cdot \left[U_y(n_x^2 + n_z^2) - U_x n_x n_y - U_z n_y n_z \right]$$

$$\cdot (n_x^2 + n_y^2 + n_z^2)^{-\frac{3}{2}}$$

$$\frac{\partial n_y}{\partial \zeta_{1x}} = \zeta_{4z} - \zeta_{2z} \qquad (43)$$

$$\frac{\partial \frac{U^n}{U^c}}{\partial n_z} = \frac{\partial \left(\frac{U_x n_1 + U_y n_2 + U_z n_3}{U_x \tau_1 + U_y \tau_2 + U_z \tau_3} \right)}{\partial n_z} \tag{44}$$

$$= \frac{1}{U^c} \left(U_x \frac{\partial n_1}{\partial n_z} + U_y \frac{\partial n_2}{\partial n_z} + U_z \frac{\partial n_3}{\partial n_z} \right)$$

$$= \frac{1}{U^c} \cdot \left[U_z(n_x^2 + n_y^2) - U_x n_x n_z - U_y n_y n_z \right]$$

$$\cdot (n_x^2 + n_y^2 + n_z^2)^{-\frac{3}{2}}$$

$$\frac{\partial n_z}{\partial \zeta_{1x}} = \zeta_{2y} - \zeta_{4y} \tag{45}$$

Substituting Eq. (40)–(45) into Eq. (37), the analytical sensitivity term $\frac{\partial \mathbf{G}_1}{\partial \zeta_b}$ is obtained. With the same method applied, $\frac{\partial \mathbf{G}_1}{\partial \zeta_b}$ can be derived similarly after substituting Eq. (47)~(48) into Eq. (46),

$$\frac{\partial \mathbf{G}_1}{\partial \dot{\zeta}_{bx}} = \frac{\partial \mathbf{G}_1}{\partial \cos \alpha} \cdot \frac{\partial \cos \alpha}{\partial \alpha} \cdot \frac{\alpha}{\partial \frac{U^n}{U^c}}$$

$$\cdot \left(\frac{\partial \frac{U^n}{U^c}}{\partial U^n} \cdot \frac{\partial U^n}{\partial U_x} \cdot \frac{\partial U_x}{\partial \dot{\zeta}_{bx}} + \frac{\partial \frac{U^n}{U^c}}{\partial U^c} \cdot \frac{\partial U^c}{\partial U_x} \cdot \frac{\partial U_x}{\partial \dot{\zeta}_b} \right)$$

$$= b_k c_k \left(-\sin\left(\tan^{-1} \frac{U^n}{U^c} \right) \right) \left(\frac{1}{1 + (\frac{U^c}{U^c})^2} \right)$$

$$\cdot \frac{\partial \frac{U^n}{U^c}}{\partial U_x} \cdot \frac{\partial U_x}{\partial \dot{\zeta}_b} \tag{46}$$

$$\frac{\partial \frac{U^n}{U^c}}{\partial U_x} = \frac{n_1(\tau_1 U_x + \tau_2 U_y + \tau_3 U_z) - \tau_1(n_1 U_x + n_2 U_y + n_3 U_z)}{(U^c)^2}$$

$$= \frac{n_1 U^c - \tau_1 U^n}{(U^c)^2} \tag{47}$$

$$\frac{\partial U_x}{\partial \dot{\zeta}_{bx}} = \frac{1}{4} \cdot \begin{bmatrix} 1 & 1 & 1 & 1 \end{bmatrix} \tag{48}$$

Other terms like $\frac{\partial \mathbf{U}_{1(2)}}{\partial \zeta_b}$ and $\frac{\partial \mathbf{U}_{1(2)}}{\partial \zeta_b}$ can not be obtained straightly through chain rules, either. For panel k, its non-circulatory velocity $\mathbf{U}_k$ is decided by $\dot{\zeta}_b$ of corner points, while its tangential vectors $\boldsymbol{\tau}^c$ and $\boldsymbol{\tau}^s$ are decided by ζ_b of the corner points, as shown in Eq. (14), Eq. (15) and Fig. 3. However, one may follow the procedures of computing $\frac{\partial \mathbf{G}_1}{\partial \zeta_b}$ and $\frac{\partial \mathbf{G}_1}{\partial \zeta_b}$ to finally obtain the sensitivity terms.

$$\frac{\partial \mathbf{U}_1}{\partial \dot{\zeta}_{bx}} = \frac{\partial \mathbf{U}_1}{\partial \mathbf{U}_k \boldsymbol{\tau}_k^c} \cdot \frac{\partial \mathbf{U}_k \boldsymbol{\tau}_k^c}{\partial \mathbf{U}_k} \cdot \frac{\partial \mathbf{U}_k}{\partial \dot{\zeta}_{bx}} \tag{49}$$

$$= \frac{1}{c_k} \frac{\partial (U_x \tau_1 + U_y \tau_2 + U_z \tau_3)}{\partial U_x} \cdot \frac{\partial U_x}{\partial \dot{\zeta}_{bx}}$$

$$= \frac{1}{4 c_k} \tau_1 \begin{bmatrix} 1 & 1 & 1 & 1 \end{bmatrix}$$

$$\frac{\partial \mathbf{U}_1}{\partial \zeta_{bx}} = \frac{\partial \mathbf{U}_1}{\partial (\mathbf{U}_k + \mathbf{u}_k^w) \boldsymbol{\tau}_k^c} \cdot \frac{\partial (\mathbf{U}_k + \mathbf{u}_k^w) \boldsymbol{\tau}_k^c}{\partial \tau_x} \cdot \frac{\partial \tau_x}{\partial \zeta_{bx}} \tag{50}$$

$$= \frac{1}{c_k} \frac{\partial (U_x \tau_1 + U_y \tau_2 + U_z \tau_3 + u_x^w \tau_1 + u_y^w \tau_2 + u_z^w \tau_3)}{\partial \tau_x}$$

$$\cdot \frac{\partial \tau_x}{\partial \zeta_{bx}}$$

$$= \frac{1}{c_k} \left[(U_x + u_x^w)(\tau_y^2 + \tau_z^2) - (U_y + u_y^w) \tau_x \tau_y \right.$$

$$\left. - (U_z + u_z^w) \tau_x \tau_z \right]$$

$$\cdot (\tau_x^2 + \tau_y^2 + \tau_z^2)^{-\frac{3}{2}} \begin{bmatrix} -\frac{1}{2} & -\frac{1}{2} & \frac{1}{2} & \frac{1}{2} \end{bmatrix}$$

$$\frac{\partial \mathbf{L}}{\partial \boldsymbol{\Gamma}_w} = \frac{\partial \mathbf{L}}{\partial \mathbf{U}_1} \cdot \frac{\partial \mathbf{U}_1}{\partial \boldsymbol{\Gamma}_w} + \frac{\partial \mathbf{L}}{\partial \mathbf{U}_2} \cdot \frac{\partial \mathbf{U}_2}{\partial \boldsymbol{\Gamma}_w} \tag{51}$$

$$= \rho \mathbf{G}_1 \mathbf{E}_1 \boldsymbol{\Gamma}_b \cdot \frac{\partial \mathbf{U}_1}{\partial \boldsymbol{\Gamma}_w} + \rho \mathbf{G}_1 \mathbf{E}_2 \boldsymbol{\Gamma}_b \cdot \frac{\partial \mathbf{U}_2}{\partial \boldsymbol{\Gamma}_w}$$

$$\frac{\partial \mathbf{U}_1}{\partial \boldsymbol{\Gamma}_w} = \frac{\partial \mathbf{U}_1}{\partial \mathbf{W}_{bw}^c \boldsymbol{\Gamma}_w} \cdot \frac{\partial \mathbf{W}_{bw}^c \boldsymbol{\Gamma}_w}{\partial \boldsymbol{\Gamma}_w} = \frac{\mathbf{W}_{bw}^c}{c_k} \tag{52}$$

$$\frac{\partial \mathbf{U}_2}{\partial \boldsymbol{\Gamma}_w} = \frac{\partial \mathbf{U}_2}{\partial \mathbf{W}_{bw}^s \boldsymbol{\Gamma}_w} \cdot \frac{\partial \mathbf{W}_{bw}^s \boldsymbol{\Gamma}_w}{\partial \boldsymbol{\Gamma}_w} = \frac{\mathbf{W}_{bw}^s}{b_k} \tag{53}$$

4. Numerical examples

As mentioned in the literature review, the beam-based modeling for flexible aircraft has been quite popular in previous studies. 3D beam elements can efficiently describe plunge and pitch movements, and both plunge and pitch movements are essential in the studies on aeroelasticity and flight dynamics. Meanwhile the FEM model of an aircraft can be constructed conveniently due to the simplicity of beam elements. On the other hand, the FEM model based on shell elements is recognized as a high fidelity tool to simulate structures that are not slender as beam elements. In this paper, both beam-based and shell-based wing models with a high aspect ratio are studied. The aeroelastic response under UVLM aerodynamic loads is obtained by applying a time-marching transient analysis scheme, which is illustrated in Fig. 4. With the vortex shedding, structural deformation and the distribution of aerodynamic forces can be observed. Thus the aerodynamic sensitivities are computed after the UVLM model is linearized around a steady state. Finally, the sensitivity results obtained by the proposed analytical solution are validated by the finite difference method.

4.1. Euler-Bernoulli beam-based flexible wing

Consider a slender isotropic beam whose geometric and physical properties are listed in Table 1. This beam-based wing model is also studied in Ref. [50] to explore the modeling technique for very flexible aircraft. The full wing structure is discretized into eight Euler-Bernoulli beam elements, in which each node has five degree-of-freedoms including z directional translation and rotation, x directional translation and rotation, y directional rotation. The lifting surface of UVLM is meshed to have eight bound vortex panels spanwise and three vortex panels chordwise, respectively. The time-marching aeroelastic analysis is conducted based on Newmark-β algorithm after coupling structure FEM and UVLM.

The unsteady vortex lattice method is firstly verified with lift coefficients. Fig. 5 compares the life coefficients within a range of angles of attack. It implies that lift coefficients of larger aspect ratios are closer to the theoretical value $2\pi\alpha$ of a wing with infinite aspect ratio. Moreover, the lift coefficient results of this beam-based wing are verified by other aerodynamic routines, including software AVL based on extended VLM and the Lifting Line Theory (LLT). It is obvious that coefficients from these three methods have little relative errors, as shown in Fig. 5.

The transient response analysis of the beam-based flexible wing model is also verified. The wingtip deformation under a nodal sinusoidal vertical force is presented in Fig. 6. It can be easily observed that the wingtip response shows a good correspondence with results obtained by MSC. Nastran.

After a beam spline interpolation algorithm is applied to couple the FEM and UVLM aerodynamics, the time-domain aeroelastic analysis is implemented. With the initial angle of attack set to be 10°, Fig. 7 shows the structural motion and wake propagation of the flexible wing in a 30 m/s freestream. The time increments used are both $\Delta t = 0.002$ s in structure and UVLM simulation.

Consider the aeroelastic state at $t = 1.0$ s as an equilibrium condition, analytical aerodynamic sensitivities can be acquired based
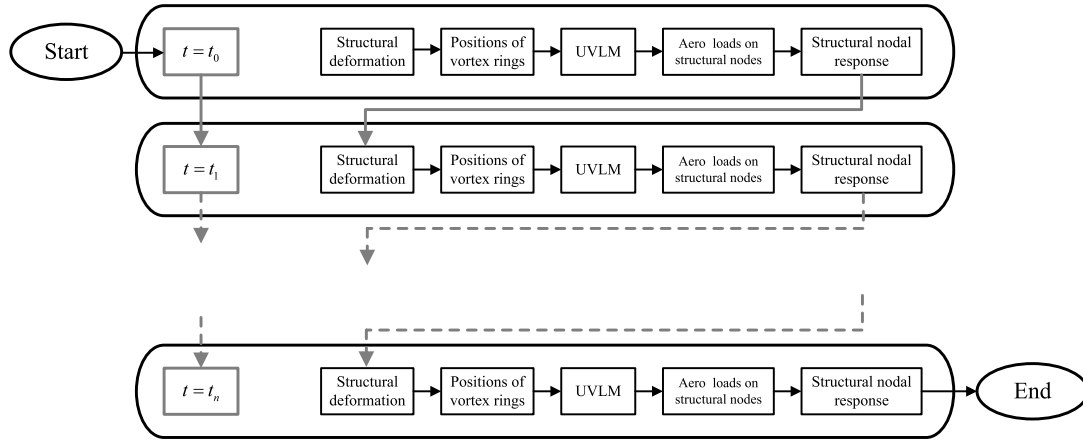
Fig. 4. Time-marching transient response analysis for an aeroelastic system with UVLM aerodynamics.

Table 1
Properties of the isotropic beam-based flexible wing model.

Properties	Value	Unit
Mass per span (m)	0.10	kg/m
Span (b)	1.00	m
Rotational moment of inertia (I_{xx})	1.30×10^{-4}	kg·m
Flat bending moment of inertia (I_{yy})	5.00×10^{-6}	kg·m
Edge bending moment of inertia (I_{zz})	1.25×10^{-4}	kg·m
Extensional rigidity ($K_{11} = EA$)	1.00×10^{6}	N
Torsional rigidity ($K_{22} = GJ$)	80.0	N·m²
Flat bending rigidity ($K_{33} = EI_y$)	50.0	N·m²
Edge bending rigidity ($K_{44} = EI_z$)	1.25×10^{3}	N·m²
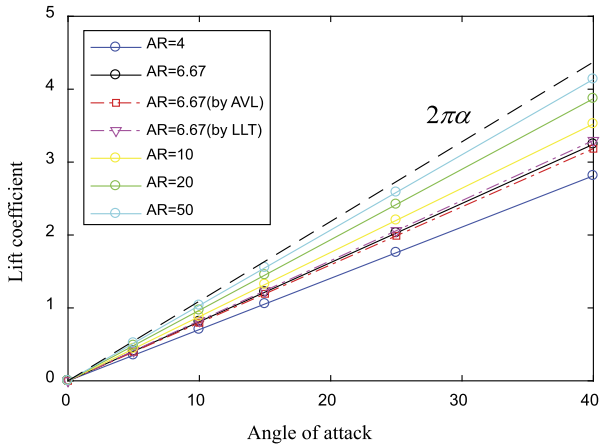
Fig. 5. Lift coefficients with change of wing aspect ratio.
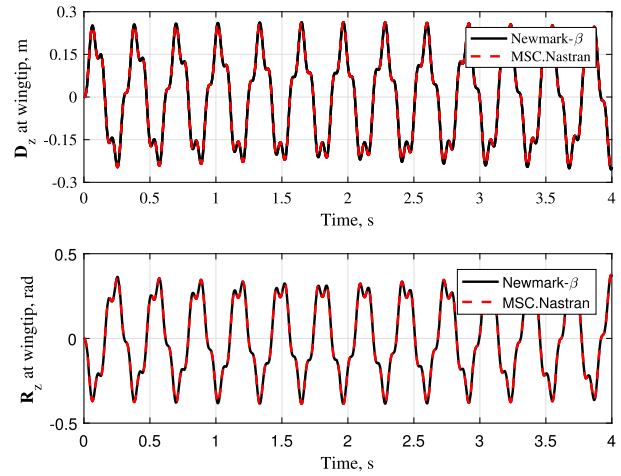
Fig. 6. Wingtip response of the beam-based flexible wing under sinusoidal loads.

Fig. 7. Boundary vortices and wake propagation of the beam-based flexible wing at $t = 0.1$s, $\Delta t = 0.002$ s.

on the derivations with chain rules. For the aeroelastic system whose FEM is established with beam elements, motions of chordwise vortex panels are interpolated from the deformation of corresponding beam elements. For vortex panels of a certain row, the angles of attack α are all same as the pitch angle of the beam element. Thus matrix $\mathbf{G}_1$ in Eq. (12) is easy to obtain. In addition, normal and tangent vectors of bound panels have linear relations with the nodal DOFs of beam elements, which makes $\mathbf{U}_1$, $\mathbf{U}_2$ and their derivatives $\frac{\partial \mathbf{U}_1}{\partial \zeta_b}$ and $\frac{\partial \mathbf{U}_1}{\partial \zeta_b}$ available for Eq. (36). Therefore, it is quite straightforward to implement the analytical sensitivity analysis in this sample case.

Here the lift sensitivity with respect to circulation strengths of bound vortex panels $\mathbf{\Gamma}_b$ is presented. In Fig. 8, every colorbar with index (i, j) indicates the impact of the change of circulation strength in jth bound vortex panel on the aerodynamic lift applied in ith 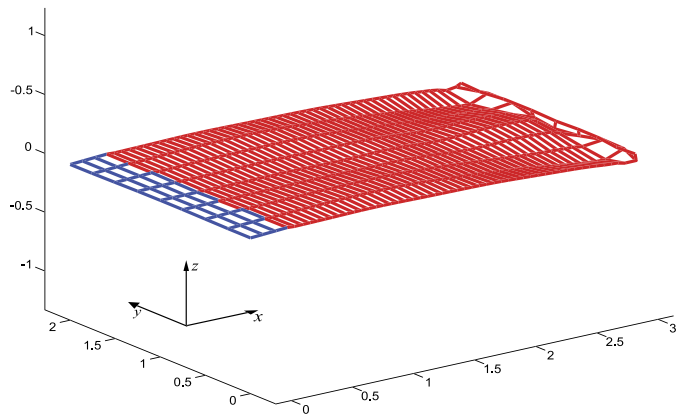bound vortex panel. As can be observed, there are two main diagonal lines with larger values. Positive values aligned along the main diagonal line represent the decisive influence that each vortex panel performs on its own distributed aerodynamic lift. Similarly, there are elements with large negative values aligned along the second diagonal line, indicating that vortex panels can also significantly affect the aerodynamic loads applied on their chordwise adjacent panels.

This numerical study shows good compatibility of the proposed analytical sensitivity analysis framework with the beam-based FEM
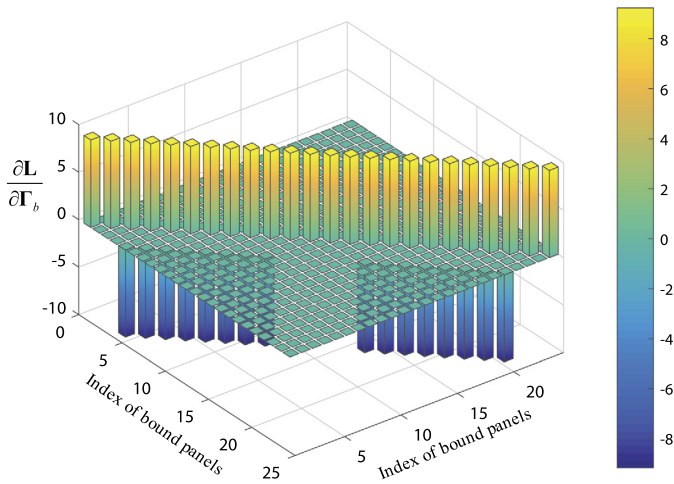
Fig. 8. Lift sensitivity with respect to circulation strengths of bound vortices in beam-based flexible wing.
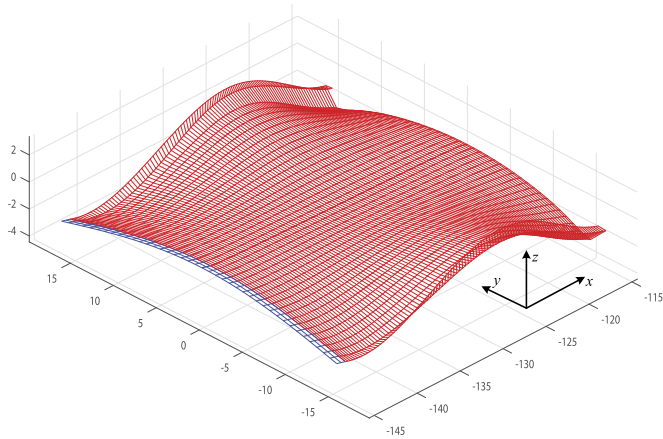

Fig. 9. Boundary vortices and wake propagation of the shell-based wing model at $t = 5$s, $\Delta t = 0.01$ s.

model, which has been widely used for modeling flexible aircraft. Detailed sensitivity results discussions are presented in the next numerical cases, which emphasizes more advantages of the pro-

posed scheme applied in flexible aircraft models with higher fidelity.

4.2. High Aspect-ratio FEM wing model with shell elements

In this simulation, a high aspect-ratio rectangular wing with a 32 m span and a 1 m chord is placed in the 30 m/s freestream with an angle of attack 5°. The wing is established with shell elements in MSC. Nastran then coupled with UVLM code for time domain aeroelastic analysis. Each wing member is discretized into 20 elements in the spanwise direction and 2 elements in the chordwise direction. The lifting surface shares the same mesh scheme with structure. The detailed numbering scheme of the boundary and wake vortices is illustrated in Fig. 10. The right wing member includes the first 40 boundary panels and 63 corner points, with the index number increasing from wing root to tip. The numbering scheme of the left wing member is symmetrical to the right member.

By using the same time-marching technique described in Fig. 4, aeroelastic response of the shell-based FEM wing can be obtained. With the time increment $\Delta t = 0.01$ s, the vortex shedding and free wake model at the end of 5 s are illustrated in Fig. 9. As those wake vortices far away from bound vortex panels only cause minor influence on aerodynamic loads, the wake model is limited to have a maximum 100 rows of shedding vortices. Theoretically, the aeroelastic sensitivities can be calculated at every specific time step. However, only those calculated around the equilibrium condition are useful for further aeroelastic stability study. Therefore, all the following sensitivity calculations and studies are performed at $t = 5$ s step, which is recognized as a steady state.

4.2.1. Aerodynamic sensitivities with respect to structural motions ζ_b and $\dot{\zeta}_b$

In the time-marching response analysis procedure, the motions of aerodynamic corner points ζ_b are obtained from the motions of all structural nodes $\mathbf{X}_s$ at every time step. The transfer matrix $\mathbf{T}$ between ζ_b and $\mathbf{X}_s$ is computed based on the thin-plate spline scheme. For the lift, a deformed bound vortex ring causes the changing of normal ($\mathbf{n}_k$) and tangential vectors ($\boldsymbol{\tau}_k^c$ and $\boldsymbol{\tau}_k^s$) of the panel k. This leads to the changing of angle of attack α_k and weighted velocity matrices $\mathbf{U}_1$, $\mathbf{U}_2$. Fig. 11 and Fig. 12 illustrate the aerodynamic lift sensitivities with respect to ζ_b in x and z-direction, respectively. In this case, there are 80 collocation points and 126 aerodynamic corner points of the bound vortex
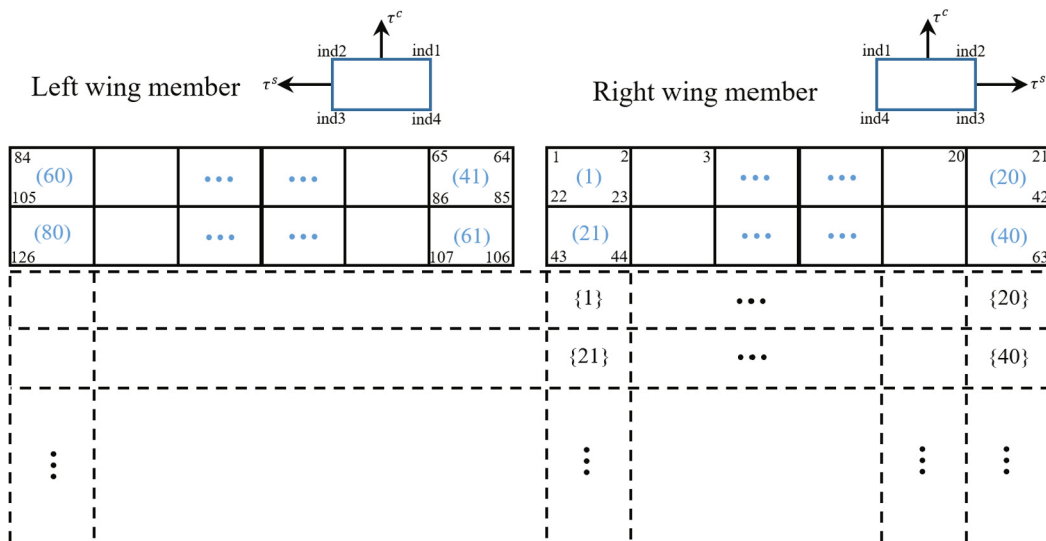

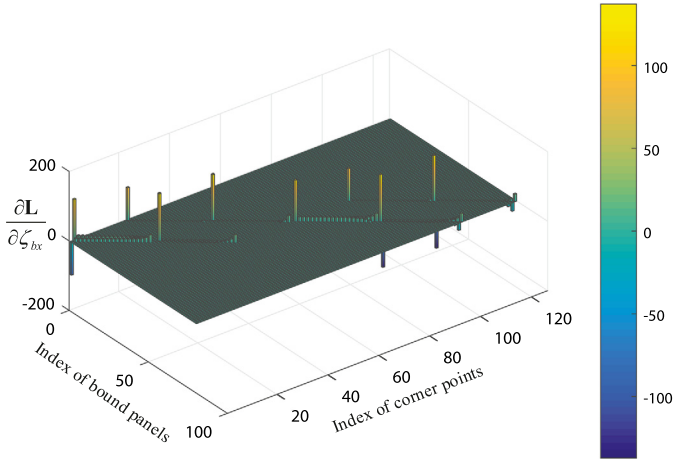**Fig. 10.** The numbering scheme of the boundary and wake vortices.
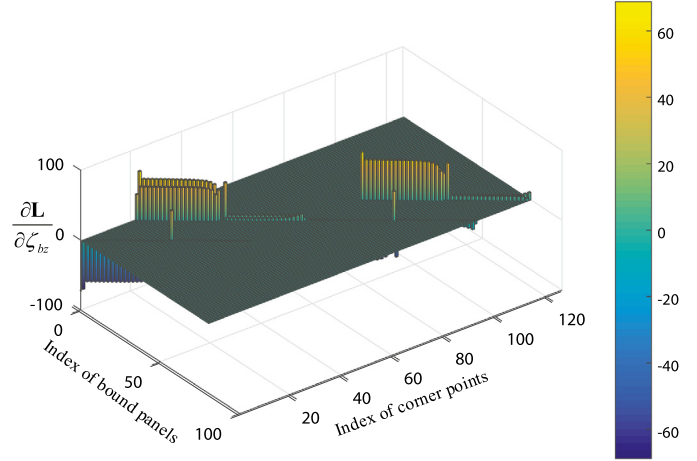
Fig. 11. Lift sensitivity with respect to ζ_{bx}.

Fig. 12. Lift sensitivity with respect to ζ_{bz}.

panels. Therefore the dimension of $\frac{\partial \mathbf{L}}{\partial \zeta_b}$ at each direction should be (80×126). Each column of the sensitivity matrix indicates the lift variation with a specific corner point being perturbed. One can easily get the Sensitivity matrix with respect to structural deformation $\mathbf{X}_s$ after multiplying $\frac{\partial \mathbf{L}}{\partial \zeta_b}$ by $\mathbf{T}$.

Similarly, the velocities of corner points $\dot{\zeta}_b$ determine the non-circulatory velocities at collocation points. The non-circulatory velocities are demonstrated to be the main cause to change the aerodynamic loads $\mathbf{L}$ and $\mathbf{D}$ through the weighted velocity matrices $\mathbf{U}_{1(2,3)}$. As plotted in Fig. 13, $\frac{\partial \mathbf{L}}{\partial \dot{\zeta}_{bz}}$ is also a (80 × 126) sparse matrix, with every element in the matrix indicating the influence of each z-directional velocity of a corner point on lift forces. A bar with the index (i,j) indicates the derivative of lift force distributed on ith panel with respect to the velocity of jth corner point. As can be observed in Fig. 13, sensitivity values of $\frac{\partial \mathbf{L}}{\partial \dot{\zeta}_{bz}}$ decrease along with the index of bound vortex panels from wing root to tip. Moreover, lift sensitivities from the trailing edge of the wing (panel index 21 to 40, 61 to 80) are considerably smaller than those from leading edge of the wing (panel index 1 to 20, 41 to 60), which also matches the general lift distribution on rectangular wings.

Sensitivity results about ζ_b and $\dot{\zeta}_b$ are both validated by finite difference method. For example, Fig. 14 shows the relative error of $\frac{\partial \mathbf{L}}{\partial \dot{\zeta}_{bz}}$ between analytical and FD calculation with $\Delta \dot{\zeta}_b = 0.001$. It is observed that relative errors of all entries in the matrix are smaller than 0.0015%. For further details, some of the specific entries of the relative error matrices are listed in Table 2 and 3. All the relative error entries whose value are smaller than 1×10^{-6} are displayed as 0 in the tables. The maximum errors are 0.0642% of the index (15,16) for $\frac{\partial \mathbf{L}}{\partial \dot{\zeta}_{bz}}$ and 0.0053% of the index (1,1) for $\frac{\partial \mathbf{L}}{\partial \dot{\zeta}_{bx}}$, respectively. From the results comparison and error analysis, it is believed that the analytical aerodynamic sensitivity analysis framework presented in this paper is accurate and effective.

4.2.2. Aerodynamic sensitivities with respect to circulation strengths of vortices Γ_b, $\dot{\Gamma}_b$ and Γ_w

As mentioned in previous sensitivity derivations based on chain rules, $\frac{\partial \mathbf{L}}{\partial \Gamma_b}$, $\frac{\partial \mathbf{L}}{\partial \Gamma_w}$ and $\frac{\partial \mathbf{L}}{\partial \dot{\Gamma}_b}$ shown in Eq. (36) represent the impact of circulation strengths of all vortex panels on the distributed aerodynamic loads. Once the aerodynamic mesh of the structure is determined, sensitivity terms $\frac{\partial \mathbf{L}}{\partial \Gamma_b}$ and $\frac{\partial \mathbf{L}}{\partial \dot{\Gamma}_b}$ will both be square matrices with the same dimension decided by the total number of bound vortex panels. However, the dimension of matrix $\frac{\partial \mathbf{L}}{\partial \Gamma_w}$ increases with time as the wake propagation proceed. Generally the free wake model is limited to a certain scale to compromise with computation cost. In this sample case, $\frac{\partial \mathbf{L}}{\partial \Gamma_b}$ and $\frac{\partial \mathbf{L}}{\partial \dot{\Gamma}_b}$ are both (80 × 80)
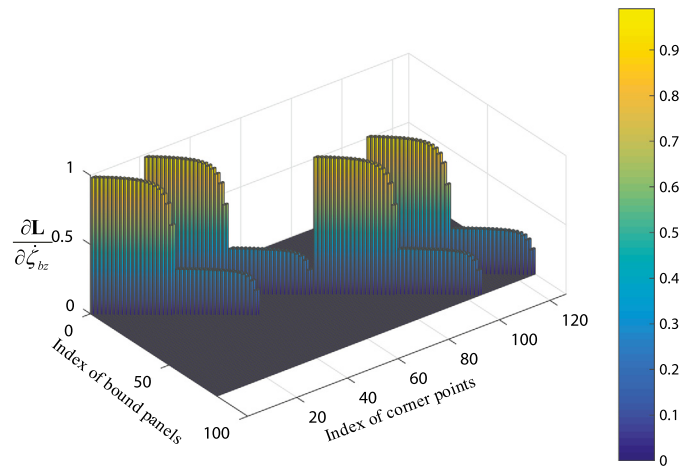

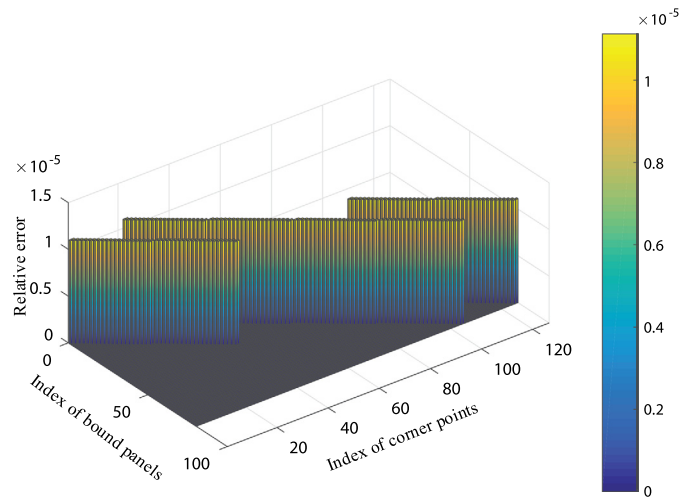**Fig. 13.** Lift sensitivity with respect to $\dot{\zeta}_{bz}$.

Fig. 14. Relative error matrix of $\frac{\partial \mathbf{L}}{\partial \dot{\zeta}_{bz}}$.

matrices based on the current wing panel discretization, which are illustrated in Fig. 15 and 16, respectively. $\frac{\partial \mathbf{L}}{\partial \Gamma_b}$ is a matrix with non-zero values aligned along the primary and secondary diagonal lines, as observed in Fig. 15. This implies that the circulation strength of kth panel Γ_b^k only affect its own vortex ring and the adjacent rings, in both spanwise and chordwise direction. Because of

Table 2
Sensitivity results comparison of $\frac{\partial \mathbf{L}}{\partial \zeta_b}$ between AN and FD methods.

Index	$\frac{\partial \mathbf{L}}{\partial \zeta_{bx}}$			$\frac{\partial \mathbf{L}}{\partial \zeta_{by}}$			$\frac{\partial \mathbf{L}}{\partial \zeta_{bz}}$		
	AN	FD	$\varepsilon(\%)$	AN	FD	$\varepsilon(\%)$	AN	FD	$\varepsilon(\%)$
(1,2)	−94.74	−94.74	0.0032	4.363×10^{-3}	-4.461×10^{-3}	0.0448	−37.25	−37.25	0.0028
(9,9)	10.40	10.40	0.0041	−0.0836	−0.0836	0.0012	−57.63	−57.63	0.0035
(15,16)	13.68	13.68	0	−0.1293	−0.1293	0	−48.06	−48.06	0.0642
(20,21)	−5.421	−5.420	0.018	0.3449	0.3449	0.0020	−38.60	−38.60	0.0078
(35,36)	2.797	2.796	0.036	−0.0598	−0.0598	0.0016	−7.123	−7.123	0.0010
(48,71)	14.88	14.88	0.0010	0.0722	0.0722	0	−57.67	−57.67	0
(60,84)	24.18	24.18	0	−0.3449	−0.3448	0.0290	−43.15	−43.15	0.0305
(70,94)	2.466	2.466	0.0065	0.0359	0.0359	0.0025	−4.012	−4.012	0.0170
(80,104)	−20.99	−20.99	0	−0.1330	−0.1330	0	−11.00	−11.00	0.0003

Table 3
Results comparison of aerodynamic sensitivities with respect to $\dot{\zeta}_b$.

Index	$\frac{\partial \mathbf{L}}{\partial \dot{\zeta}_{bx}}$			$\frac{\partial \mathbf{L}}{\partial \dot{\zeta}_{bz}}$			$\frac{\partial \mathbf{D}}{\partial \dot{\zeta}_{bz}}$		
	AN	FD	$\varepsilon(\%)$	AN	FD	$\varepsilon(\%)$	AN	FD	$\varepsilon(\%)$
(1,1)	2.809	2.809	0.0053	0.9902	0.9902	0.0011	-1.812×10^{-4}	-1.812×10^{-4}	0.0032
(6,6)	2.800	2.800	0.0053	0.9871	0.9871	0.0011	-1.781×10^{-4}	-1.781×10^{-4}	0.0032
(15,15)	2.687	2.687	0.0053	0.9482	0.9482	0.0011	-1.630×10^{-4}	-1.630×10^{-4}	0.0032
(34,36)	0.9010	0.9010	0.0052	0.3181	0.3181	0.0011	-8.541×10^{-5}	-8.541×10^{-5}	0.0031
(60,84)	1.851	1.851	0.0052	0.6532	0.6532	0.0011	-1.126×10^{-4}	-1.126×10^{-4}	0.0030
(75,121)	0.8897	0.8897	0.0052	0.3142	0.3142	0.0011	-9.066×10^{-5}	-9.066×10^{-5}	0.0030
(80,126)	0.5231	0.5231	0.0052	0.1851	0.1851	0.0011	-3.830×10^{-5}	-3.830×10^{-5}	0.0030
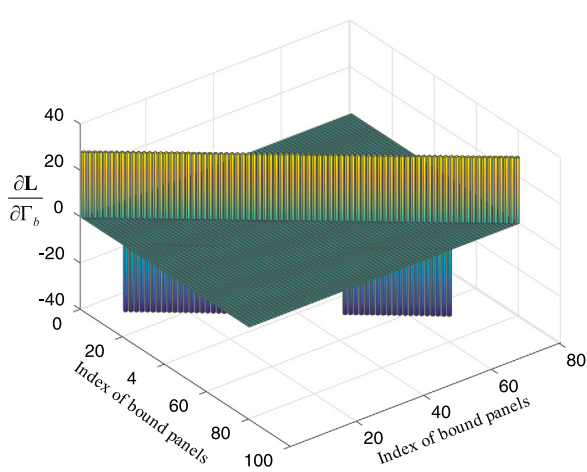
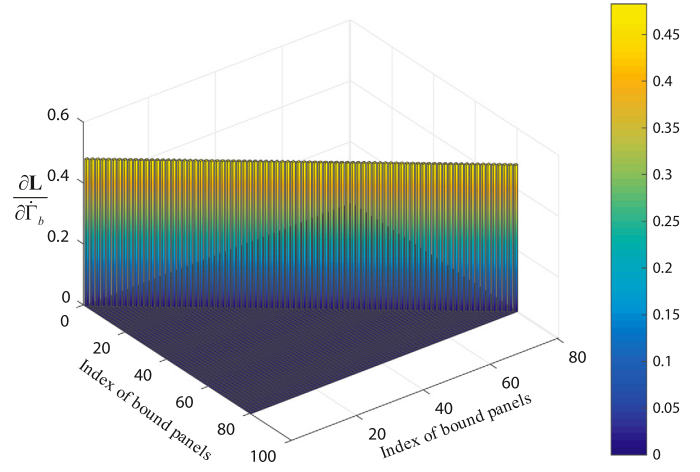**Fig. 15.** Lift sensitivity with respect to $\mathbf{\Gamma}_b$.

Fig. 16. Lift sensitivity with respect to $\dot{\mathbf{\Gamma}}_b$.

the vortex rings shedding mechanism, the impact of Γ_b^k on its next spanwise $(k+1)$th vortex ring is much smaller than on adjacent $(k+m)$th vortex ring along with chordwise direction. For example, the self-influence and chordwise-influence sensitivity values are $\frac{\partial \mathbf{L}}{\partial \mathbf{\Gamma}_b}|_{(6,6)} = 28.49$ and $\frac{\partial \mathbf{L}}{\partial \mathbf{\Gamma}_b}|_{(26,6)} = -28.50$ respectively, while the spanwise-influence sensitivity value is $\frac{\partial \mathbf{L}}{\partial \mathbf{\Gamma}_b}|_{(7,6)} = 0.0065$. For any other entry that is not adjacent to the sixth vortex panel, such as $\frac{\partial \mathbf{L}}{\partial \mathbf{\Gamma}_b}|_{(3,6)}$ or $\frac{\partial \mathbf{L}}{\partial \mathbf{\Gamma}_b}|_{(80,6)}$, its value will be 0. The sensitivity matrices for aerodynamic drag have the similar phenomenon, but they are not plotted in this paper to avoid content redundancy.

Results of sensitivity $\frac{\partial \mathbf{L}}{\partial \dot{\mathbf{\Gamma}}_b}$ is plotted in Fig. 16. According to Eq. (12), there is only one coefficient matrix $\rho \mathbf{G}_1$ in the computational relation from $\dot{\mathbf{\Gamma}}_b$ to $\mathbf{L}$. Therefore, it is reasonable that the sensitivity matrix is diagonal with similar values aligned along the diagonal line when the structural is not highly deformed, as observed in Fig. 16.

For the calculation of sensitivities with respect to circulation strengths of wake vortices $\mathbf{\Gamma}_w$, the maximum layer number of wake vortex model is set to be 100 for the reduction of computational cost. Thus the size of sensitivity term $\frac{\partial \mathbf{L}}{\partial \mathbf{\Gamma}_w}$ is considerably

large as (80×4000). Therefore, Fig. 17 only shows the first 60 discretized elements in the matrix of $\frac{\partial \mathbf{L}}{\partial \mathbf{\Gamma}_w}$, which represent the impact of first two rows of the wake vortices. In addition, several entries of $\frac{\partial \mathbf{L}}{\partial \mathbf{\Gamma}_w}$ are selected and listed in Table 4 to show the whole picture about the wake influence. Note that all the sensitivity values that are smaller than 1×10^{-6} are displayed as 0.

Results indicate that the distance between wake and bound vortex panels plays a key role to affect the aerodynamic sensitivity. The distributed aerodynamic loads are much more sensitive to wake vortices that are close to the trailing edge of the structure. For example, elements with index (39,19), (38,18) and (37,17) from the first row of the wake have the biggest values in the whole matrix of $\frac{\partial \mathbf{L}}{\partial \mathbf{\Gamma}_w}$, as shown in Fig. 17 and Table 4. On the other hand, the elements with index (9,400), (1,2233), (50,3360) and (20,3990) have much smaller values even zero, indicating the little influence of distant wake vortices on aerodynamic loads. Therefore, the sensitivity analysis presented in this paper can also be used as the theoretical basis to make appropriate wake model truncation for other applications and studies with UVLM aerodynamics.

Table 4
Sensitivity results of $\frac{\partial \mathbf{L}}{\partial \mathbf{\Gamma}_w}$ obtained by AN method.

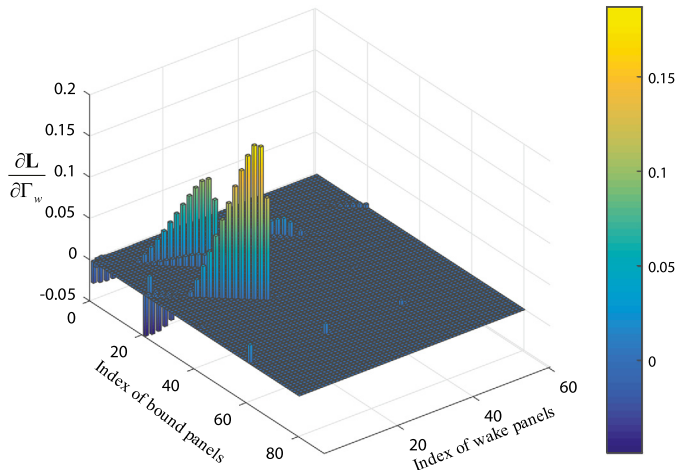| Index (front)	Sensitivity value	Index (middle)	Sensitivity value	Index (rear)	Sensitivity value
(1,1)	-0.0258	(1,183)	2.842×10^{-4}	(1,2233)	2.8129×10^{-5}
(36,16)	0.1562	(21,185)	1.7290×10^{-4}	(9,2258)	0
(39,19)	0.1859	(19,278)	-5.7280×10^{-4}	(50,3000)	-5.0014×10^{-5}
(61,21)	0.0134	(42,336)	-1.0095×10^{-5}	(66,3360)	-5.4345×10^{-6}
(38,57)	-0.0058	(20,352)	-4.5368×10^{-5}	(20,3990)	0
(15,115)	-0.0012	(9,400)	-1.1415×10^{-4}	(1,4000)	-4.4397×10^{-6}

Fig. 17. Analytical lift sensitivity with respect to circulation strengths of wake vortices.

The analytical sensitivity results including $\frac{\partial \mathbf{L}}{\partial \mathbf{\Gamma}_b}$, $\frac{\partial \mathbf{L}}{\partial \mathbf{\Gamma}_w}$ and $\frac{\partial \mathbf{L}}{\partial \hat{\mathbf{\Gamma}}_b}$ are all validated by the finite difference method. Similar with previous error analysis for $\frac{\partial \mathbf{L}}{\partial \zeta_b}$ and $\frac{\partial \mathbf{L}}{\partial \zeta_b}$, the largest relative errors for $\frac{\partial \mathbf{L}}{\partial \mathbf{\Gamma}_b}$, $\frac{\partial \mathbf{L}}{\partial \mathbf{\Gamma}_w}$ and $\frac{\partial \mathbf{L}}{\partial \hat{\mathbf{\Gamma}}_b}$ between these two methods are all under 0.1%. Therefore the aerodynamic sensitivity analysis with respect to the circulation strengths of vortices are demonstrated to be effective.

5. Conclusion

This paper has detailed an efficient scheme to obtain the aerodynamic sensitivities with respect to both structural deformation and circulation strengths of vortices for highly flexible aircraft. These sensitivities were computed analytically based on the chain rule with UVLM aerodynamics. In the section of numerical studies, the proposed analytical sensitivity analysis approach was applied in both beam-based and shell-based flexible wing models to prove its technical versatility. From the transient response of aerostructure coupling systems, aerodynamic sensitivities were computed around the equilibrium condition. The impact of the bound and wake vorticities on the aerodynamic loads was then revealed. It showed that distributed aerodynamic loads were much more sensitive to wake vortices that are close to the trailing edge. In addition, this paper also studied the aerodynamic sensitivities with respect to the warping of bound vortex panels. It turned out that the displacements of vortex rings along the normal vector direction contributed more to aerodynamic loads distributed on the lifting surface. The analytical results were all validated by the numerical results calculated via the finite difference method. The formulations derived in this paper provide the foundation for developing a time-domain aeroelastic analysis framework that is adequate for next-generation flexible aerial vehicles. Calculated aerodynamic sensitivities can be used for further studies on stability analysis and gradient-based optimization.

Declaration of competing interest

There is no conflict of interest on our submitted manuscript.

References

[1] T. Kier, Comparison of unsteady aerodynamic modelling methodologies with respect to flight loads analysis, in: AIAA Atmospheric Flight Mechanics Conference and Exhibit, 2005, p. 6027.
[2] E. Albano, W.P. Rodden, A doublet-lattice method for calculating lift distributions on oscillating surfaces in subsonic flows, AIAA J. 7 (2) (1969) 279–285.
[3] Z. Chen, Y. Zhao, R. Huang, Parametric reduced-order modeling of unsteady aerodynamics for hypersonic vehicles, Aerosp. Sci. Technol. 87 (2019) 1–14.
[4] Q. Zhou, G. Chen, A. Da Ronch, Y. Li, Reduced order unsteady aerodynamic model of a rigid aerofoil in gust encounters, Aerosp. Sci. Technol. 63 (2017) 203–213.
[5] M. Winter, F.M. Heckmeier, C. Breitsamter, Cfd-based aeroelastic reduced-order modeling robust to structural parameter variations, Aerosp. Sci. Technol. 67 (2017) 13–30.
[6] G. Seber, O.O. Bendiksen, Nonlinear flutter calculations using finite elements in a direct eulerian-lagrangian formulation, AIAA J. 46 (6) (2008) 1331–1341.
[7] Z. Lyu, J.R. Martins, Aerodynamic design optimization studies of a blended-wing-body aircraft, J. Aircr. 51 (5) (2014) 1604–1617.
[8] G.K. Kenway, J.R. Martins, Multipoint high-fidelity aerostructural optimization of a transport aircraft configuration, J. Aircr. 51 (1) (2014) 144–160.
[9] M.J. Patil, D.H. Hodges, C.E.S. Cesnik, Nonlinear aeroelasticity and flight dynamics of high-altitude long-endurance aircraft, J. Aircr. 38 (1) (2001) 88–94.
[10] C.M. Shearer, C.E. Cesnik, Nonlinear flight dynamics of very flexible aircraft, J. Aircr. 44 (5) (2007) 1528–1545.
[11] W. Su, C.E.S. Cesnik, Nonlinear aeroelasticity of a very flexible blended-wing-body aircraft, J. Aircr. 47 (5) (2010) 1539–1553.
[12] X.-Z. Gao, Z.-X. Hou, Z. Guo, J.-X. Liu, X.-Q. Chen, Energy management strategy for solar-powered high-altitude long-endurance aircraft, Energy Convers. Manag. 70 (2013) 20–30.
[13] N. Tsushima, W. Su, Flutter suppression for highly flexible wings using passive and active piezoelectric effects, Aerosp. Sci. Technol. 65 (2017) 78–89.
[14] N. Tsushima, W. Su, A study on adaptive vibration control and energy conversion of highly flexible multifunctional wings, Aerosp. Sci. Technol. 79 (2018) 297–309.
[15] V.M. Falkner, The calculation of aerodynamic loading on surfaces of any shape, Tech. rep., AERONAUTICAL RESEARCH COUNCIL LONDON (UNITED KINGDOM), 1943.
[16] S.G. Hedman, Vortex lattice method for calculation of quasi steady state loadings on thin elastic wings in subsonic flow, Tech. rep., AERONAUTICAL RESEARCH INST OF SWEDEN STOCKHOLM, 1966.
[17] D.T. Mook, A.H. Nayfeh, Application of the vortex-lattice method to high-angle-of-attack subsonic aerodynamics, SAE Transact. (1985) 517–532.
[18] J.M. Elzebda, D.T. Mook, A.H. Nayfeh, Numerical simulation of steady and unsteady, vorticity-dominated aerodynamic interference, J. Aircr. 31 (5) (1994) 1031–1036.
[19] V.J. Rossow, Validation of vortex-lattice method for loads on wings in lift-generated wakes, J. Aircr. 32 (6) (1995) 1254–1262.
[20] S. Fiddes, J. Gaydon, A new vortex lattice method for calculating the flow past yacht sails, J. Wind Eng. Ind. Aerodyn. 63 (1–3) (1996) 35–59.

[21] S. Haghighat, J.R. RA Martins, H.H.T. Liu, Aeroservoelastic design optimization of a flexible wing, J. Aircr. 49 (2) (2012) 432–443.

[22] C. Xie, L. Wang, C. Yang, Y. Liu, Static aeroelastic analysis of very flexible wings based on non-planar vortex lattice method, Chin. J. Aeronaut. 26 (3) (2013) 514–521.

[23] B.F. Ng, H. Hesse, R. Palacios, J.M.R. Graham, E.C. Kerrigan, Aeroservoelastic state-space vortex lattice modeling and load alleviation of wind turbine blades, Wind Energy 18 (7) (2015) 1317–1331.

[24] O.Ş. Gabor, A. Koreanschi, R.M. Botez, A new non-linear vortex lattice method: applications to wing aerodynamic optimizations, Chin. J. Aeronaut. 29 (5) (2016) 1178–1195.

[25] M. Parenteau, É. Laurendeau, G. Carrier, Combined high-speed and high-lift wing aerodynamic optimization using a coupled vlm-2.5 d rans approach, Aerosp. Sci. Technol. 76 (2018) 484–496.

[26] J. Katz, A. Plotkin, Low-Speed Aerodynamics, vol. 13, Cambridge university press, 2001.

[27] R. Karkehabadi, Aerodynamic interference of a large and a small aircraft, J. Aircr. 41 (6) (2004) 1424–1429.

[28] C. Sequeira, D. Willis, J. Peraire, Comparing aerodynamic models for numerical simulation of dynamics and control of aircraft, in: 44th AIAA Aerospace Sciences Meeting and Exhibit, 2006, p. 1254.

[29] B.D. Hall, D.T. Mook, A.H. Nayfeh, S. Preidikman, Novel strategy for suppressing the flutter oscillations of aircraft wings, AIAA J. 39 (10) (2001) 1843–1850.

[30] Z. Wang, P. Chen, D. Liu, D. Mook, M. Patil, Time domain nonlinear aeroelastic analysis for hale wings, in: 47th AIAA/ASME/ASCE/AHS/ASC Structures, Structural Dynamics, and Materials Conference 14th AIAA/ASME/AHS Adaptive Structures Conference 7th, 2006, p. 1640.

[31] T. Lambert, G. Dimitriadis, Induced drag calculations with the unsteady vortex lattice method for cambered wings, AIAA J. 55 (2) (2016) 668–672.

[32] B. Stanford, P. Beran, Formulation of analytical design derivatives for nonlinear unsteady aeroelasticity, AIAA J. 49 (3) (2011) 598–610.

[33] B. Obradovic, K. Subbarao, Modeling of flight dynamics of morphing wing aircraft, J. Aircr. 48 (2) (2011) 391–402.

[34] S. Chen, H. Li, S. Guo, M. Tong, B. Ji, Unsteady aerodynamic model of flexible flapping wing, Aerosp. Sci. Technol. 80 (2018) 354–367.

[35] A.T. Nguyen, J.-H. Han, Wing flexibility effects on the flight performance of an insect-like flapping-wing micro-air vehicle, Aerosp. Sci. Technol. 79 (2018) 468–481.

[36] Z. Wang, P.C. Chen, D.D. Liu, D.T. Mook, Nonlinear-aerodynamics/nonlinear-structure interaction methodology for a high-altitude long-endurance wing, J. Aircr. 47 (2) (2010) 556–566.

[37] W. Su, Y. Huang, J.R. Hammerton, Nonlinear aeroelasticity of highly flexible joined-wing aircraft using unsteady vortex-lattice method, in: 58th AIAA/ASCE/AHS/ASC Structures, Structural Dynamics, and Materials Conference, 2017, p. 1353.

[38] Z. Rong, B. Cao, J. Hu, Stability analysis on an aeroelastic system for design of a flutter energy harvester, Aerosp. Sci. Technol. 60 (2017) 203–209.

[39] L.N. Long, T.E. Fritz, Object-oriented unsteady vortex lattice method for flapping flight, J. Aircr. 41 (6) (2004) 1275–1290.

[40] R. Palacios, J. Murua, R. Cook, Structural and aerodynamic models in nonlinear flight dynamics of very flexible aircraft, AIAA J. 48 (11) (2010) 2648–2659.

[41] J. Murua, R. Palacios, J.M.R. Graham, Assessment of wake-tail interference effects on the dynamics of flexible aircraft, AIAA J. 50 (7) (2012) 1575–1585.

[42] J. Murua, R. Palacios, J.M.R. Graham, Applications of the unsteady vortex-lattice method in aircraft aeroelasticity and flight dynamics, Prog. Aerosp. Sci. 55 (2012) 46–72.

[43] K.C. Hall, Eigenanalysis of unsteady flows about airfoils, cascades, and wings, AIAA J. 32 (12) (1994) 2426–2432.

[44] I.R. Chittick, J.R. Martins, An asymmetric suboptimization approach to aerostructural optimization, Optim. Eng. 10 (1) (2009) 133.

[45] B. Stanford, P. Ifju, Aeroelastic topology optimization of membrane structures for micro air vehicles, Struct. Multidiscip. Optim. 38 (3) (2009) 301–316.

[46] D. Murthy, K. Kaza, Application of a semianalytical technique for sensitivity analysis of unsteady aerodynamic computations, in: Advanced Marine Systems Conference, 1988, p. 2377.

[47] R. Kolonay, V. Venkayya, H.T.Y. Yang, Sensitivity analysis for transonic unsteady aeroelastic constraints, J. Aircr. 35 (4) (1998) 574–581.

[48] W.-L. Li, E. Livne, Analytic sensitivities and approximations in supersonic and subsonic wing/control surface unsteady aerodynamics, J. Aircr. 34 (3) (1997) 370–379.

[49] B.K. Stanford, P.S. Beran, Analytical sensitivity analysis of an unsteady vortex-lattice method for flapping-wing optimization, J. Aircr. 47 (2) (2010) 647–662.

[50] W. Su, C.E. Cesnik, Strain-based geometrically nonlinear beam formulation for modeling very flexible aircraft, Int. J. Solids Struct. 48 (16–17) (2011) 2349–2360.